PLOS ONE

RESEARCH ARTICLE

Exosomal miRs in Lung Cancer: A Mathematical Model

Xiulan Lai[1]*, **Avner Friedman**[2]

1 Institute for Mathematical Sciences, Renmin University of China, Beijing, P. R. China, **2** Mathematical Bioscience Institute & Department of Mathematics, Ohio State University, Columbus, OH, United States of America

* xiulanlai@ruc.edu.cn

Citation: Lai X, Friedman A (2016) Exosomal miRs in Lung Cancer: A Mathematical Model. PLoS ONE 11(12): e0167706. doi:10.1371/journal.pone.0167706

Editor: Moray Campbell, Roswell Park Cancer Institute, UNITED STATES

Received: March 30, 2016

Accepted: November 18, 2016

Published: December 21, 2016

Data Availability Statement: All relevant data are within the paper.

Funding: AF is supported by the Mathematical Biosciences Institute and the National Science Foundation (Grant DMS 0931642). XL is supported by the National Natural Science Foundation of China (Grant No. 11501568), the Fundamental Research Funds for the Central Universities and the Research Funds of Renmin University of China, and the Mathematical Biosciences Institute and the National Science Foundation (Grant DMS 0931642).

Abstract

Lung cancer, primarily non-small-cell lung cancer (NSCLC), is the leading cause of cancer deaths in the United States and worldwide. While early detection significantly improves five-year survival, there are no reliable diagnostic tools for early detection. Several exosomal microRNAs (miRs) are overexpressed in NSCLC, and have been suggested as potential biomarkers for early detection. The present paper develops a mathematical model for early stage of NSCLC with emphasis on the role of the three highest overexpressed miRs, namely miR-21, miR-205 and miR-155. Simulations of the model provide quantitative relationships between the tumor volume and the total mass of each of the above miRs in the tumor. Because of the positive correlation between these miRs in the tumor tissue and in the blood, the results of the paper may be viewed as a first step toward establishing a combination of miRs 21, 205, 155 and possibly other miRs as serum biomarkers for early detection of NSCLC.

Introduction

Lung cancer is the leading cause of cancer-related deaths in the United States and worldwide, and non-small cell lung cancer (NSCLC) constitutes 85% of lung cancer deaths [1, 2]. Five years survival rate for NSCLC is significantly higher for those diagnosed at early stage [3], but there are no reliable tools for early detection of lung cancer. Most lung cancers are first diagnosed on symptoms. Approximately 10% of patients present brain metastasis at the time of initial diagnosis and their mean survival is 4 months [4]. Hence, there is a need for novel noninvasive biomarkers for early lung cancer diagnosis [5].

Exosomes are nano-vesicles of size 30-100 nm in diameter, surrounded by a lipid bilayer, and containing fuctional proteins, mRNAs and microRNAs (miRs). Exosomes are released by various cells, including cancer cells [6]. A growing body of evidence suggests that exosomal miRs may be used as serum biomarkers for prognosis of malignant tumors [5, 7]. Furthermore, exosomal miRs inhibitors have been evaluatedas anti-tumor drugs in experimental and clinical work for several types of cancer, including lung cancer [8, 9].

Competing Interests: The authors have declared that no competing interest exist.

In the present paper we develop a mathematical model that relates the role of the exosomal miRs in lung cancer tissue to cancer cells proliferation and invasion. Since there is a positive correlation between exosomal miRs in serum and tissue in lung cancer [10–12], the model may serve as a first step toward establishing miRs as reliable serum biomarkers for early detection.

A simple schematic of a cell proliferation in the context of cancer is shown in Fig 1. When epidermal growth factor (EGF) ligands to its receptor EGFR, it initiates activation of the Ras-Raf-MEK-ERK pathway [13, 14] and the PI3K-AKT pathway [15–17]. Both pathways lead to cell proliferation [18–21] through activation of mTOR [16, 20, 22]. EGF-EGFR is negatively regulated by ERK [14, 23].

EGFR tyrosine kinase inhibitor (TKI) modulates the activation of both RAS and PI3K, thereby inhibiting the activation of the downstream pathways of EGF-EGFR [13, 24, 25]. PTEN modulates the activation of AKT through converting PIP3, generated by PI3K, to PIP2 by dephosphorylation [15]. When DNA damage occurs, a signaling pathway activates Apaf-1

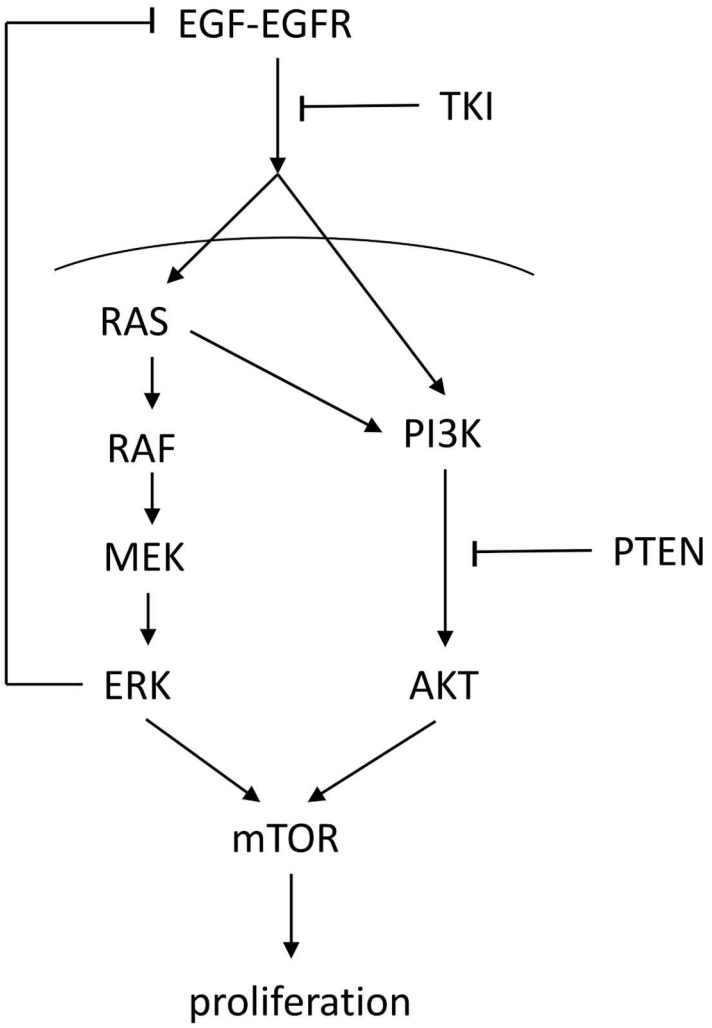

Fig 1. Two pathways, Ras-Raf-MEK-ERK and PI3K-AKT lead to the cell proliferation. Sharp arrows indicate activation/enhancement and blocked arrows indicate inhibition.

doi:10.1371/journal.pone.0167706.g001

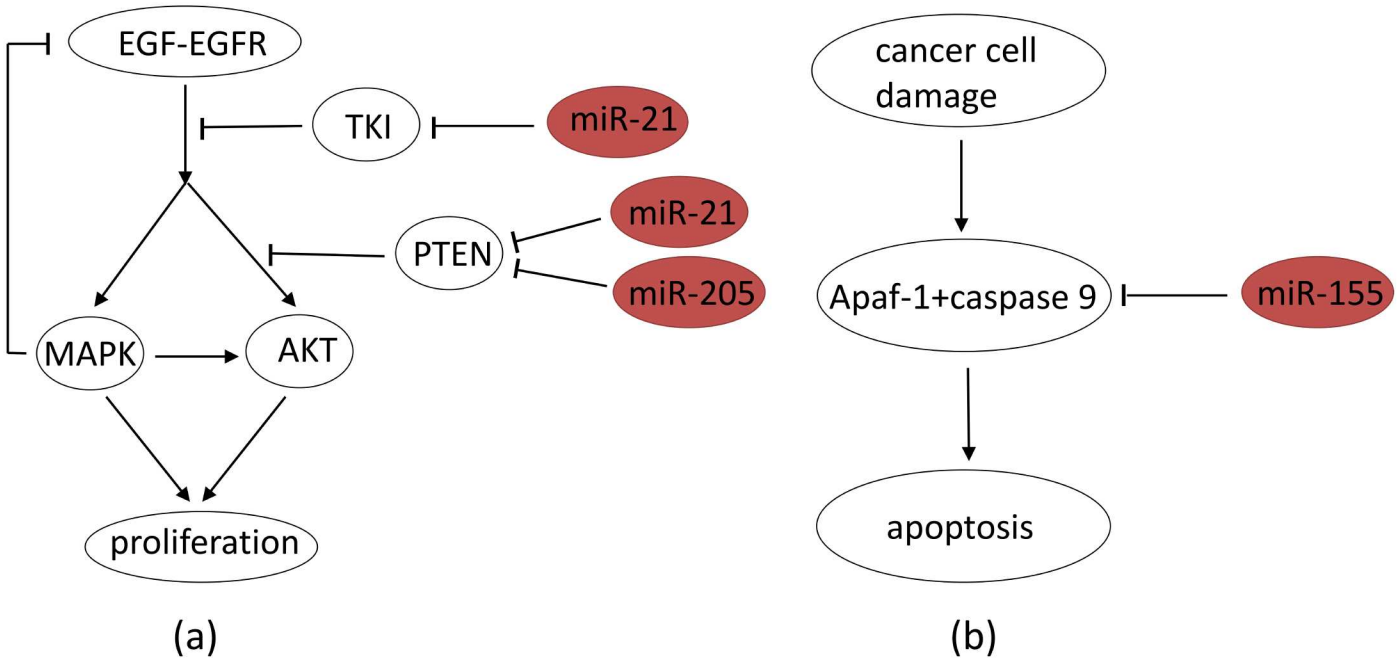

Fig 2. Abbreviated version of Fig 1 depicting the roles of miR-21, miR-205 and miR-155. MAPK represents the Ras-Raf-MEK-ERK signaling pathway and AKT represents the PI3K-AKT signaling pathway. (a) MiR-21 blocks TKI; miR-21 and miR-205 block PTEN. (b) MiR-155 blocks Apaf-1 +caspase 9. Sharp arrows indicate activation/enhancement and blocked arrows indicate inhibition.

doi:10.1371/journal.pone.0167706.g002

and caspase 9, forming an apoptosome, which leads to apoptosis through activation of caspase 3 [26, 27].

In NSCLC, the most expressed exosomal miRs are miR-21, miR-155 and miR-205 [10]. In Fig 2(a), we simplified the network of Fig 1 by using MAPK and AKT to represent the Ras-Raf-MEK-ERK and PI3K-AKT pathways. Fig 2(a) also shows the effect of overexpression of miR-21 and miR-205 on NSCLC proliferation. Recent studies established that miR-21 blocks TKI [8, 25], and thus promotes activation of the MAPK and AKT pathways. Also, miR-21 and miR-205 block PTEN [28, 29] and thus promote the activation of the AKT-mTOR pathway. Fig 2(b) shows the effect of overexpression of miR-155. MiR-155 blocks Apaf-1 expression [30] and thus also cellular apoptosis when DNA damage occurs. Hence overexpressions of miR-21 and miR-205 give rise to uncontrolled proliferation, while overexpression of miR-155 leads to reduced apoptosis. MiR-21 and miR-205 have also other targets; in particular it was suggested that miR-21 targets tumor suppressors involved in apopotsis, including Apaf-1, Pdcd4, RhoB and Faslg [31, 32]; hence overexpression of miR-21 reduces apoptosis. However, for simplicity, we focus in this paper on what seems to be the main targets of miR-21 and miR-205 in NSCLC, as shown in Fig 2.

In this paper we consider growth and invasion of lung tumor associated with mutations in EGFR, MAPK and AKT, and its treatment by anti exosomal miRNAs (miR-21, miR-205 and miR-155). We use the mathematical model to determine the efficacy of these drugs under these mutations.

We consider two aspects of tumor progression: (i) Invasion, in which a tumor planar front progresses, in time, away from the main body of the tumor; (ii) Proliferation, in which a small spherical tumor grows in time. In order to focus on the role of the exosomal-miRs, we do not

include in the model the immune responses and angiogenesis; thus the model represents an early stage of lung cancer.

Mathematical model

The mathematical model is based on the network shown in Fig 2. For simplicity we use just one variable, MAPK, to represent the Ras-Raf-MEK-ERK signaling pathway, and AKT to represent the PI3K-AKT signaling pathway. We also combine miR-205 with miR-21 in modeling their effect on blocking PTEN. Table 1 lists the variables used in the mathematical model in unit of g/cm^3.

Equations for proteins As in [33], the dynamics $\frac{d\vec{y}}{dt} = \vec{f}(\vec{y})$ of the proteins within cancer cells will appear in the form

$$\frac{d\vec{y}}{dt} = \vec{f}(\vec{y})\frac{C}{C_0},$$

where C_0 is the steady state density of cancer cells.

Equation for EGF-EGFR (*E*). The equation for EGF-EGFR is given by

$$\frac{dE}{dt} = \left[\lambda_E \cdot \frac{1}{1 + M/K_{ME}} - d_E E\right]\frac{C}{C_0}. \quad (1)$$

The coefficient λ_E is the production rate of the EGF-EGFR complex and the factor $1/(1 + M/K_{ME})$ is the inhibition by ERK [14]; d_E is the degradation rate of E.

Equation for MAPK (*M*). The MAPK pathway is activated by the EGF-EGFR [13, 14], a process resisted by TKI [8, 13]. Hence

$$\frac{dM}{dt} = \left[\lambda_M E \cdot \frac{1}{1 + T/K_{TM}} - d_M M\right]\frac{C}{C_0}, \quad (2)$$

where d_M is the degradation rate of M.

Equation for AKT (*A*). The activation of the AKT pathway initiates with the activation of PI3K (P_3) by EGF-EGFR directly and also through Ras (which is activated by EGF-EGFR) [15,

Table 1. List of variables in unit of g/cm^3.

Notation	Description
E	EGF-EGFR concentration
M	active MAPK concentration
P_3	PI3K concentration
A	active AKT concentration
T	TKI concentration
P	PTEN concentration
Ap	Apaf-1-caspase 9 apoptosome concnetration
E_C	cancer-shed exosome concentration
m_1	exosomal miR-21 concentration (inlcuding miR-205)
m_1^i	cellular miR-21 concentration (inlcuding miR-205)
m_2	exosomal miR-155 concentration
m_2^i	cellular miR-155 concentration
C	cancer cells density
N	normal healthy cells density

doi:10.1371/journal.pone.0167706.t001

16, 19, 20]. In view of the TKI inhibition of EFG-EGFR [24, 25], the equation for P_3 takes the form

$$\frac{dP_3}{dt} = \lambda_{P3}E \cdot \frac{1}{1+T/K_{TA}} \cdot \left(1 + \lambda_{MA}\frac{S}{K_{SP}+S}\right) - d_{P3}P_3,$$

where S is the concentration of Ras.

AKT is activated by PI3K which is negatively regulated by PTEN [15, 25], so that

$$\frac{dA}{dt} = \lambda_{AP}P_3 \cdot \frac{1}{1+P/K_{PA}} - d_A A.$$

We assume that the turnover of PI3K is very fast (the half-life of PI3K is very short [34]) and deduce from the steady state equation of P_3 that

$$P_3 = \frac{\lambda_{P3}}{d_{P3}}E \cdot \frac{1}{1+T/K_{TA}} \cdot \left(1 + \lambda_{MA}\frac{S}{K_{SP}+S}\right).$$

Substituting this into the equation for AKT, we obtain

$$\frac{dA}{dt} = \frac{\lambda_{AP}\lambda_{P3}}{d_{P3}}E \cdot \frac{1}{1+P/K_{PA}} \cdot \frac{1}{1+T/K_{TA}} \cdot \left(1 + \lambda_{MA}\frac{S}{K_{SP}+S}\right) - d_A A.$$

Assuming also that the concentration of Ras is proportional to that of MAPK, i.e. $S = \mu M$, we obtain the following equation for AKT:

$$\frac{dA}{dt} = \left[\lambda_A E \cdot \frac{1}{1+P/K_{PA}} \cdot \frac{1}{1+T/K_{TA}} \cdot \left(1 + \lambda_{MA}\frac{M}{K_{MA}+M}\right) - d_A A\right]\frac{C}{C_0}, \tag{3}$$

where $\lambda_A = \lambda_{AP}\lambda_{P3}/d_{P3}$, $K_{MA} = K_{SP}/\mu$.

Equation for TKI (T). The production of TKI is inhibited by miR-21 [8, 25]. Recalling that miR-21 is only a fraction of m_1, we write the equation for TKI in the form

$$\frac{dT}{dt} = \left[\lambda_T \cdot \frac{1}{1+1/2\cdot(m_1+m_1^i)/K_{mT}} - d_T T\right]\frac{C}{C_0}. \tag{4}$$

Equation for PTEN (P). The expression of PTEN is inhibited by both miR-21 and miR-205 [28, 29]. Hence

$$\frac{dP}{dt} = \left[\lambda_P \cdot \frac{1}{1+(m_1+m_1^i)/K_{mP}} - d_P P\right]\frac{C}{C_0}. \tag{5}$$

Equation for Apaf-1-caspase 9 apoptosome (Ap). The expression of Apaf-1 is down-regulated by miR-155 [30]. Hence

$$\frac{dAp}{dt} = \left[\lambda_{Ap} \cdot \frac{1}{1+(m_2+m_2^i)/K_{m_2}} - d_{Ap}Ap\right]\frac{C}{C_0}. \tag{6}$$

Equation for exosome (E_C). Cancer cells shed exosomes at a rate $\lambda_{Ec}C$. We assume that exosomes are degraded, releasing their miRs, when merging with cancer cells. Taking the rate of this degradation to be $d_{Ec}E_C \cdot \frac{C}{K_C+C}$, the equation for the concentration of exosomes is given

by

$$\frac{\partial E_C}{\partial t} - D_{E_C}\Delta E_C = \lambda_{E_C} C - d_{E_C} E_C \cdot \frac{C}{K_C + C}, \tag{7}$$

where the term $D_{Ec}\Delta E_C$ represents dispersion (or diffusion) of exosomes.

Equations for exosomal miR-21 (m_1) and exosomal miR-155 (m_2). MiR-21 and miR-155 are released from exosomes when exosomes merge with cancer cells. We take the exosomal production rate of miR-21 to be $\lambda_{m_1} E_C \cdot C/(K_C + C)$, and obtain the equation

$$\frac{\partial m_1}{\partial t} - D_{m_1}\Delta m_1 = \lambda_{m_1} E_C \cdot \frac{C}{K_C + C} - d_{m_1} m_1. \tag{8}$$

Similarly, the equation for miR-155 is given by

$$\frac{\partial m_2}{\partial t} - D_{m_2}\Delta m_2 = \lambda_{m_2} E_C \cdot \frac{C}{K_C + C} - d_{m_2} m_2. \tag{9}$$

Equations for miR-21 (m_1^i) and miR-155 (m_2^i) in cancer cells. Since m_1^i and m_2^i lie in cancer cells, they diffuse with same coefficient as cancer cells. Hence, the equations for m_1^i and m_2^i are given by

$$\frac{\partial m_1^i}{\partial t} - D_C\Delta m_1^i = \lambda_{m_1^i} C - d_{m_1} m_1^i, \tag{10}$$

and

$$\frac{\partial m_2^i}{\partial t} - D_C\Delta m_2^i = \lambda_{m_2^i} C - d_{m_2} m_2^i, \tag{11}$$

respectively.

We will apply the mathematical model to consider two phases of tumor progression of lung cancer, invasion and proliferation.

Model for tumor invasion

Equation for cancer cell (C) in tumor invasion. The equation for cancer cell is the following:

$$\begin{aligned} \frac{\partial C}{\partial t} - D_C\Delta C - \chi\nabla\cdot(C\nabla C) &= \left(\lambda_{C1}\frac{M}{K_M + M} + \lambda_{C2}\frac{A}{K_A + A}\right)\cdot C\left(1 - \frac{C}{C_M}\right) \\ &\quad - d_D C\cdot\frac{Ap}{K_{Ap} + Ap} - d_C C. \end{aligned} \tag{12}$$

Invasion of cancer cells is driven by competition for space and resources [35, 36]. At the early stage of tumor invasion resources are not limited, hence cells undergo migration in the direction of decreased gradient of cancer cells density. On the left-hand side of Eq (12) the term $\chi\nabla\cdot(C\nabla C)$ represents the directed migration of cancer cells in response to the competition for space; χ is the 'directed migration coefficient'. We assume a logistic growth with rate which depends on both MAPK and AKT, since both pathways lead to cell replication; this accounts for the first term on the right-hand side of Eq (12). In addition to natural apoptosis, at rate $d_C C$, damage to cancer cells (at rate proportional to $d_D C$) leads to apoptosis by formation of the Apaf-1-caspase 9 apoptosome [26, 27]; this is accounted for by the second term on the right-hand side of Eq (12).

Boundary and initial conditions for tumor invasion model. We assume that a solid tumor lies in the the half plane $x < 0$, and model the progression of the tumor front in the direction of increasing x. We assume that the tumor front is planar, and that it moves in the interval $0 \leq x \leq 2$ from $x = 0$ cm towards the end-point $x = 2$ cm. We impose the following boundary conditions for the cancer cells, exosomes and miRs:

$$\begin{cases} E_C(0,t) = E_{C0}, \quad m_1(0,t) = m_{10}, \quad m_2(0,t) = m_{20}, \quad C(0,t) = C_0, \quad \text{at } x = 0; \\ \text{no-flux at } x = 2. \end{cases} \tag{13}$$

Since initially the cancer is confined to $x < 0$, we take zero initial conditions:

$$\begin{cases} E(x,0) = M(x,0) = A(x,0) = T(x,0) = P(x,0) = Ap(x,0) = 0, \text{ and} \\ E_C(x,0) = m_1(x,0) = m_2(x,0) = 0, \; C(x,0) = 0, \quad \text{for } 0 \leq x \leq 2. \end{cases} \tag{14}$$

Model for tumor proliferation

Equations for cancer cells (*C*) and normal healthy cells (*N*) in tumor proliferation. In the tumor invasion model, the directed migration coefficient χ represents the directed movement of the invading tumor cells. The precise range of the parameter χ is unknown. In order to visualize significant advance of the migrating tumor front we took χ to be the 'relatively' large. However, in the tumor proliferation model, proliferating cells grow faster than migrating cells [37–39], and the competition for space is primarily a competition with normal healthy cells (with density N) [40]. We therefore assume that the directed movement of cells is determined by the condition that the total cell density, $C + N$, is constant at each point in the tumor. The term $-\chi\nabla \cdot (C\nabla C)$ in Eq (12) is then neglected and replaced by the term $\nabla \cdot (\mathbf{u}C)$, where $\mathbf{u}$ represents the velocity of cells. The equation for cancer cells is given by

$$\begin{aligned} \frac{\partial C}{\partial t} - D_C \Delta C + \nabla \cdot (\mathbf{u}C) \quad = \quad & \left(\lambda_{C1} \frac{M}{K_M + M} + \lambda_{C2} \frac{A}{K_A + A} \right) \cdot C \left(1 - \frac{C + \varepsilon N}{C_M} \right) \\ & - d_D C \cdot \frac{Ap}{K_{Ap} + Ap} - d_C C, \end{aligned} \tag{15}$$

where the competition for space with the normal healthy cells is represented by the term εN in the logistic growth. We assume that most exosomes shed by cancer cells release their content when they make contact with nearby cancer cells, and therefore keep Eq (7) unchanged. The equation for normal healthy cells, N, is given by

$$\frac{\partial N}{\partial t} - D_N \Delta N + \nabla \cdot (\mathbf{u}N) = \lambda_N N \left(1 - \frac{N + \varepsilon C}{C_M} \right) - d_{DN} N \cdot \frac{Ap}{K_{Ap} + Ap} - d_N N. \tag{16}$$

The competition for space with cancer cells is represented by the term εC in the logistic growth term [40].

To simplify the computations, we assume that the tumor is spherical and denote its moving boundary (i.e. its radius) by $r = R(t)$. We also assume that all the densities and concentrations are radially symmetric, that is, functions of (r, t), where $0 \leq r \leq R(t)$. In particular, $\mathbf{u} = u(r,t)\mathbf{e}_r$, where $\mathbf{e}_r$ is the unit radial vector.

Equation for *u*: We assume that the combined densities of healthy and cancer cells in the tumor is constant (θ), and take

$$N + C = \theta = 0.6 \text{ g/cm}^3. \tag{17}$$

We also assume that $D_N = D_C$. Adding Eqs (16) and (15), we obtain

$$\begin{aligned}\frac{1}{r^2}\frac{\partial}{\partial r}(r^2\theta u) &= \left[\lambda_N N\left(1-\frac{N+\varepsilon C}{C_M}\right)\right.\\ &\left.+\left(\lambda_{C1}\frac{M}{K_M+M}+\lambda_{C2}\frac{A}{K_A+A}\right)C\left(1-\frac{C+\varepsilon N}{C_M}\right)\right]\\ &-\left[(d_{DN}N+d_DC)\cdot\frac{Ap}{K_{Ap}+Ap}+(d_NN+d_CC)\right],\end{aligned}$$

so that

$$\begin{aligned}u(r,t) &= \frac{1}{\theta r^2}\int_0^r \xi^2\left[\lambda_N N\left(1-\frac{N+\varepsilon C}{C_M}\right)\right.\\ &\left.+\left(\lambda_{C1}\frac{M}{K_M+M}+\lambda_{C2}\frac{A}{K_A+A}\right)C\left(1-\frac{C+\varepsilon N}{C_M}\right)\right]d\xi\\ &-\frac{1}{\theta r^2}\int_0^r \xi^2\left[(d_{DN}N+d_DC)\cdot\frac{Ap}{K_{Ap}+Ap}+(d_NN+d_CC)\right]d\xi.\end{aligned}$$

We assume that the free boundary $r = R(t)$ moves with the velocity of cells:

$$\frac{dR(t)}{dt} = u(R(t),t). \tag{18}$$

Boundary and initial conditions for tumor proliferation model. We impose the boundary conditions:

$$\text{No-flux for } E_C(r,t),\ m_1(r,t),\ m_2(r,t),\ C(r,t) \text{ and } N(r,t) \text{ at } r = R(t). \tag{19}$$

We assume that the concentrations of proteins TKI, PTEN and Apaf-1 which inhibit tumor growth are 'relatively' high, i.e., above the steady state, so that they initially decrease as the tumor begins to increase. We also assume that the remaining proteins which are involved in promoting tumor growth, are initially below their steady state. One choice of initial conditions is given below:

$$\begin{cases} R(0) = 0.01\text{cm};\\ E(r,0) = 6.7044\times10^{-4}\text{g/cm}^3,\ M(r,0) = 7.14\times10^{-6}\text{g/cm}^3,\\ A(r,0) = 7.396\times10^{-7}\text{g/cm}^3,\ T(r,0) = 1.0206\times10^{-4}\text{g/cm}^3,\\ P(r,0) = 2.2748\times10^{-7}\text{g/cm}^3,\ Ap(r,0) = 3.4648\times10^{-5}\text{g/cm}^3,\\ E_C(r,0) = 3.6\times10^{-12}\text{g/cm}^3,\ m_1(r,0) = 2.8\times10^{-15}\text{g/cm}^3,\\ m_2(r,0) = 1.4\times10^{-15}\text{g/cm}^3,\ C(x,0) = 0.35\text{g/cm}^3,\\ N(r,0) = 0.25\text{g/cm}^3, \quad \text{for } 0\le r\le R(0).\end{cases} \tag{20}$$

Table 2. Summary of parameter values.

Notation	Description	Value used	References
D_{Ec}	diffusion coefficient of exosomes	1.23×10^{-4}cm^{2}day^{-1}	[82] & estimated
D_{m_1}	diffusion coefficient of miR-21	0.13028cm^{2}day^{-1}	[61, 83] & estimated
D_{m_2}	diffusion coefficient of miR-155	0.13028cm^{2}day^{-1}	[61, 83] & estimated
D_C	diffusion coefficient of cancer cells	8.64×10^{-7}cm^{2}day^{-1}	[77]
D_N	diffusion coefficient of normal healthy cells	8.64×10^{-7}cm^{2}day^{-1}	[77]
χ	directed migration coefficient	$3 \times 10^{-4} - 3 \times 10^{-2}$ cm^{5}g^{-1}day^{-1}	[33] & estimated
λ_E	production rate of EGF-EGFR	1.1741×10^{-3}day^{-1} g/cm^3	[47] & estimated
λ_M	production rate of MAPK	1.6499×10^{-2}day^{-1}	[47, 48] & estimated
λ_A	production rate of AKT	2.9422×10^{-3}day^{-1}	[67, 68] & estimated
λ_{MA}	activation rate of AKT by MAPK (Ras)	1/2	[75] & estimated
λ_T	production rate of TKI	8.4013×10^{-4}day^{-1} g/cm^3	estimated
λ_P	production rate of PTEN	2.3352×10^{-4}day^{-1} g/cm^3	[47, 70] & estimated
λ_{Ap}	production rate of Apaf-1	4.4095×10^{-3}day^{-1} g/cm^3	[73] & estimated
λ_{Ec}	production rate of exosome by NSCLC cells	9.81×10^{-9}day^{-1}	[58] & estimated
λ_{m_1}	production rate of miR-21 & miR-205 by E_C	0.8626×10^{-3}day^{-1}	[59, 74] & estimated
λ_{m_2}	production rate of miR-155 by E_C	0.4313×10^{-3}day^{-1}	[59, 74] & estimated
λ_{C1}	growth rate of NSCLC cells due to MAPK	0.6133 day^{-1}	[77] & estimated
λ_{C2}	growth rate of NSCLC cells due to AKT	0.3067 day^{-1}	[77] & estimated
λ_N	growth rate of normal healthy cells	0.092 day^{-1}	[77] & estimated
ε	competition for space coefficient	0.1	[40]
d_E	degradation rate of EGF-EGFR	0.8318 day^{-1}	[47] & estimated
d_M	degradation rate of MAPK	0.6931 day^{-1}	[63–66]
d_A	degradation rate of AKT	0.6931 day^{-1}	[67, 68]
d_T	degradation rate of TKI	0.3466 day^{-1}	[69] & estimated
d_P	degradation rate of PTEN	22.1807 day^{-1}	[70, 71]
d_{Ap}	degradation rate of Apaf-1	2.7726 day^{-1}	[73]
d_{Ec}	degradation rate of exosome	21.8 day^{-1}	fitted
d_{m_1}	degradation rate of miR-21 and miR-205	0.5545 day^{-1}	[74]
d_{m_2}	degradation rate of miR-155	0.5545 day^{-1}	[74]
d_C	natural death rate of cancer cells	0.023 day^{-1}	[77] & estimated
d_D	death rate of cancer cells due to DNA damage	0.414 day^{-1}	[77] & estimated
d_N	natural death rate of normal healthy cells	0.023 day^{-1}	[77] & estimated

doi:10.1371/journal.pone.0167706.t002

Results

Results for tumor invasion

In simulating the invasion of cancer cells we use the model Eqs (1)–(12), with boundary Conditions (13) and initial Conditions (14), and with the parameters of Tables 2 and 3.

We explore how specific mutations affect the invasion of the tumor front, and how anti-miR drugs slow the invasion. We consider four cases: (i) the control case (with unspecified mutations), (ii) new mutation in EGFR, (iii) new mutation in MAPK, (iv) new mutation in AKT. In the control case all the parameters are taken to be the same as Tables 2 and 3, and χ is taken to be 3×10^{-2}cm^{5}g^{-1}day^{-1}. In the case of mutations in EGFR, MAPK or AKT, χ is unchanged but the production rates λ_E, λ_M and λ_A are increased by some factor. The first row of Fig 3 shows the spatial profile of cancer cell density $C(x, t)$ in the control case, and in the

Table 3. Summary of parameter values (continued).

Notation	Description	Value used	References
E_0	S.S. [1]concentration of EGF-EGFR	7.0573×10^{-4} g/cm^3	[47]
M_0	S.S. concentration of MAPK	8.4×10^{-6} g/cm^3	[48, 50]
P_{30}	S.S. concentration of PI3K	1.56×10^{-6} g/cm^3	[53, 54]
A_0	S.S. concentration of AKT	9.362×10^{-7} g/cm^3	[53]
T_0	S.S. concentration of TKI	8.5050×10^{-5} g/cm^3	estimated
P_0	S.S. concentration of PTEN	1.88×10^{-7} g/cm^3	[47]
Ap_0	S.S. concentration of Apaf-1-caspase 9	2.84×10^{-5} g/cm^3	[57]
E_{C0}	S.S. concentration of C-shed exosome	3.6×10^{-10} g/cm^3	[58]
m_{10}	S.S. concentration of miR-21 and miR-205	2.8×10^{-13} g/cm^3	[59, 60]
m_{20}	S.S. concentration of miR-155	1.4×10^{-13} g/cm^3	[10, 59]
C_0	S.S. density of cancer cell	0.4 g/cm^3	[62]
N_0	S.S. density of normal healthy cells	0.14 g/cm^3	[62] & estimated
C_M	carrying capacity of NSCLC cells	0.8 g/cm^3	[62]
K_{ME}	inhibition of EGF-EGFR by ERK	3.936×10^{-5} g/cm^3	[53, 54] & estimated
K_{TM}	inhibition of MAPK by TKI	8.5050×10^{-5} g/cm^3	estimated
K_{TA}	inhibition of AKT by TKI	8.5050×10^{-5} g/cm^3	estimated
K_{PA}	inhibition of AKT by PTEN	1.88×10^{-7} g/cm^3	[47]
K_{mT}	inhibition of TKI by miR-21	0.56×10^{-13} g/cm^3	[59, 60] & estimated
K_{mP}	inhibition of PTEN by miR-21 and miR-205	0.56×10^{-13} g/cm^3	[59, 60] & estimated
K_{m_2}	inhibition of Apaf-1 by miR-155	0.28×10^{-13} g/cm^3	[10, 59] & estimated
K_{MA}	half-saturation of MAPK (Ras) in AKT activation	8.4×10^{-6} g/cm^3	[48, 50] & estimated
K_C	half-saturation of cancer cell on merging with exosome	0.4 g/cm^3	[62] & estimated
K_M	half-saturation of MAPK on cancer cell proliferation	8.4×10^{-6} g/cm^3	[48, 50] & estimated
K_A	half-saturation of AKT on cancer cell proliferation	9.362×10^{-7} g/cm^3	[47] & estimated
K_{Ap}	half-saturation of Apaf-1 on NSCLC cell apoptosis	2.84×10^{-5} g/cm^3	[57] & estimated

[1]S.S. refers to steady state.

doi:10.1371/journal.pone.0167706.t003

three cases of mutations (in EGFR, MAPK and AKT) at different time points $t = 5, 15, 30, 60$ days. We see that under each of the three mutations the tumor advanced at day 60 by at least 10% more than in the control case. We note however that although the sizes of the invasion under the three mutations are nearly the same, we accounted for the three mutations differently, increasing the production rates of EGFR by a factor 1.3, of MAPK by a factor 1.6 and of AKT by a factor 1.8. The ratios between these factors suggest that a mutation of EGFR increases tumor invasion more than a mutation of MAPK, and a mutation of MAPK increases tumor invasion more than a mutation of AKT. These suggestions, however, need to be verified experimentally.

The second row of Fig 3 shows the effect of anti-miR-21 drug in the control case and in the cases of EGFR, MAPK and AKT mutations. We note that anti-miR-21 reduces the rate of invasion by approximately 17%. When both anti-miR-21 and anti-miR-155 are combined, the reduction is by 40%, as seen in the third row of Fig 3.

Fig 4 simulates the dynamics of the total linear mass of the cancer cells in the control case and the cases of the three mutations when (i) no drug is applied, (ii) anti-miR-21 is applied, and (iii) both anti-miR-21 and anti-miR-155 are applied. We see that, by day 60: (i) each mutation increased the total cancer linear mass by approximately 25% compared to the control

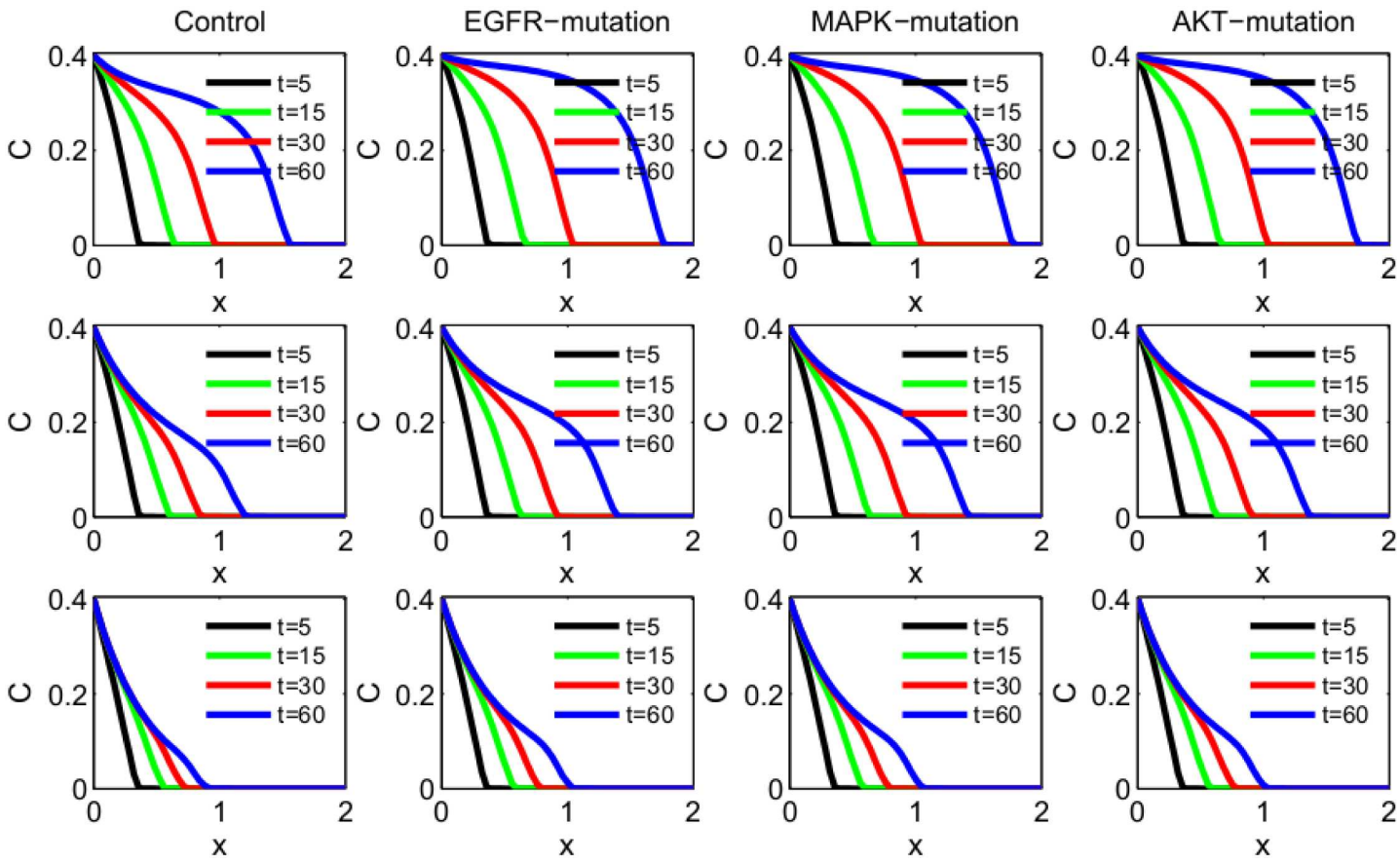

Fig 3. Invasion of cancer cells with density $C(x, t)$. The parameters are as in Tables 2 and 3, and $\chi = 3 \times 10^{-2}$ cm^{5}g^{-1}day^{-1}. (a) The first row: The control case; a mutation in EGFR where λ_E is increased by 1.3-fold; a mutation in MAPK where λ_M is increased by 1.6-fold; a mutation in AKT where λ_E is increased by 1.8-fold. (b) The second row: Using anti-miR-21, where λ_{m_1} is reduced by a factor 2 compared to the first row. (c) The third row: Using both anti-miR-21 and anti-miR-155, where λ_{m1} and λ_{m2} are reduced by a factor 2 compared to the first row. The time is in unit of day, and x is in unit of cm.

doi:10.1371/journal.pone.0167706.g003

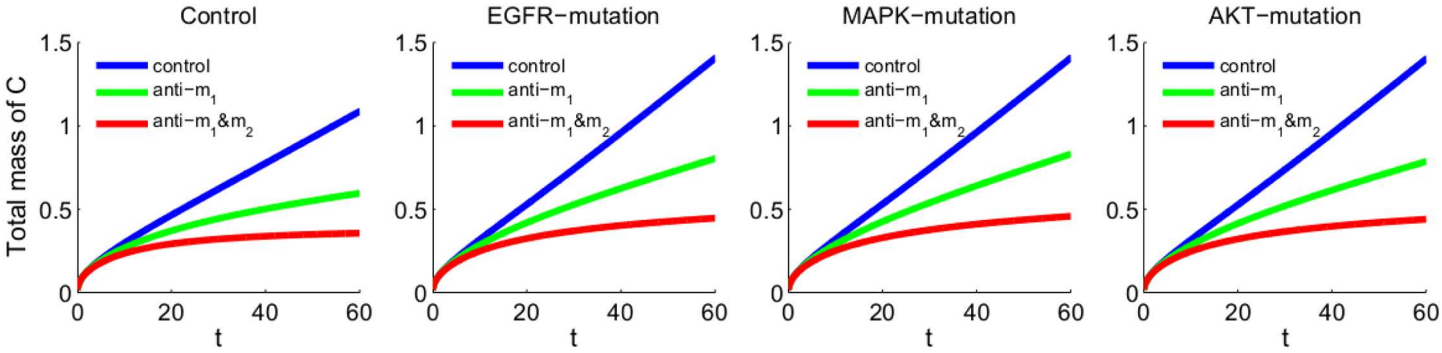

Fig 4. Total linear mass of cancer cells. The mutations and anti-miRs are the same as in Fig 3, and all parameters are the same as in Fig 3. In the legend, anti-m_1 indicates anti-miR-21, and anti-m_1&m_2 indicates the combination of anti-miR-21 and anti-miR-155. The time is in unit of day, and the mass is in unit of g.

doi:10.1371/journal.pone.0167706.g004

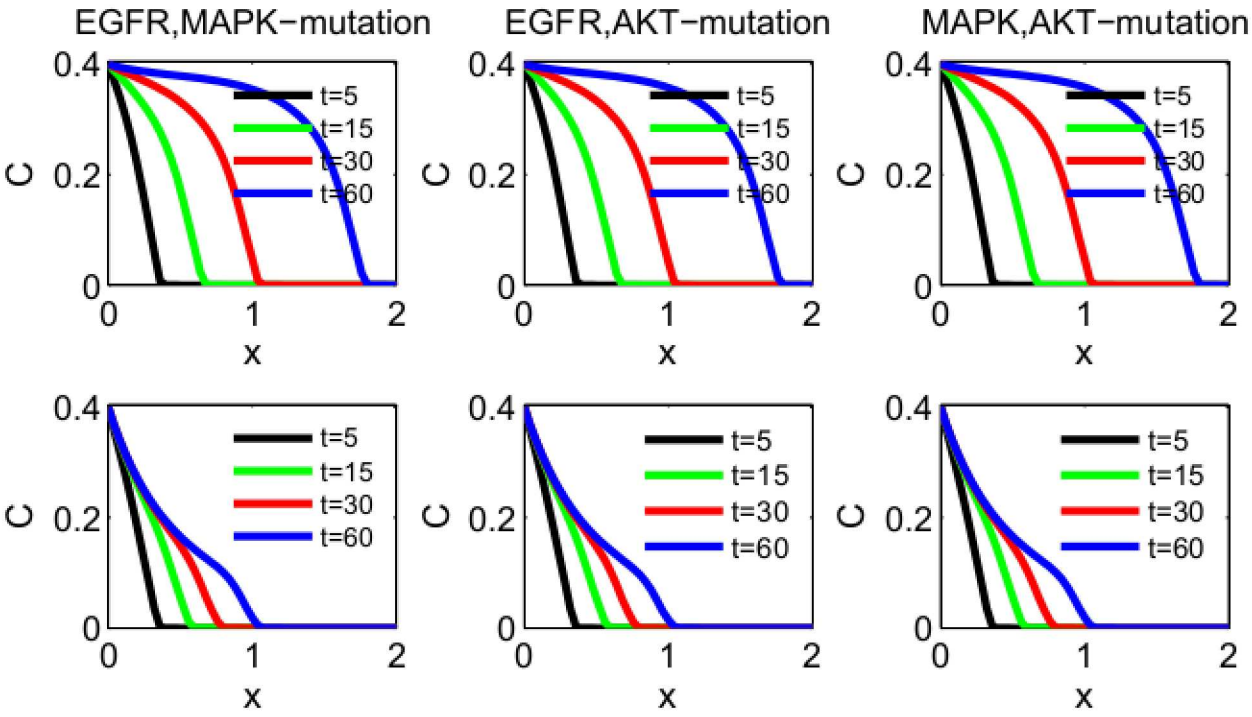

Fig 5. Invasion of cancer cells with density *C*(*x*, *t*). The parameters are as in Tables 2 and 3, and $\chi = 3 \times 10^{-2}$ cm^{5}g^{-1}day^{-1}. (a) Mutations in both EGFR and MAPK, where λ_E and λ_M are increased by 1.15-fold and 1.3-fold, respectively; mutations in both EGFR and AKT, where λ_E and λ_A are increased by 1.15-fold and 1.4-fold, respectively; mutations in both MAPK and AKT, where λ_M and λ_A are increased by 1.3-fold and 1.4-fold, respectively. (b) Using both anti-miR-21 and anti-miR-155, where both λ_{m_1} and λ_{m_2} are reduced by a factor 2 compared to the panels in (a). The time is in unit of days, and *x* is in unit of cm.

doi:10.1371/journal.pone.0167706.g005

case; (ii) anti-miR-21 reduced the total tumor linear mass by approximately 40%; and (iii) in combination with anti-miR-155 the reduction was 65%, and the total linear tumor mass did not grow faster than in the untreated control case.

Similar results can be obtained in the case of multiple mutations. Fig 5 illustrates the case of two mutations (the first row), with reduction in invasion front by approximately 40% at day 60 when the cancer is treated with both anti-miR-21 and anti-miR-155 drugs (the second row).

Cancer invasion depends on the directed migration coefficient χ. In [33] the range of the parameter χ was taken to be $(3 \times 10^{-4}, 3 \times 10^{-2})$cm^{5}g^{-1}day^{-1}. In the simulations of Figs 3–5, we took the largest value $\chi = 3 \times 10^{-2}$cm^{5}g^{-1}day^{-1} in order to visualize the invasion of the tumor front over a relatively short period of time. It is reasonable to expect that both tumor invasion and total mass will decrease if χ is decreased. This is illustrated in Fig 6 in the case of a tumor with the same EGFR mutation as in Figs 3 and 4. We denote by R_χ the distance traveled by the tumor front by day 60, and by M_χ the total linear mass of the cancer cells by day 60. Fig 6 shows the growth of R_χ and M_χ (at day 60) as χ increases from 3×10^{-4} to 3×10^{-2}cm^{5}g^{-1}day^{-1}: R_χ increases by a factor 8 and M_χ increases by a factor 11 approximately.

We next apply anti-miR-21 and anti-miR-155 drugs to the tumor (by reducing λ_{m_1} and λ_{m_2} to $\lambda_{m_1}/2$ and $\lambda_{m_2}/2$, as in Figs 3 and 4) and denote the corresponding R_χ and M_χ by R_χ^m and M_χ^m. We represent the efficacy of the anti-miRs drugs by $\phi_R := (R_\chi - R_\chi^m)/R_\chi$ and $\phi_M := (M_\chi - M_\chi^m)/M_\chi$, that is, by the percentage of reduction in R_χ and M_χ. Fig 7 shows that the efficacy of the drug increases as the directed migration coefficient χ increases. The efficacy

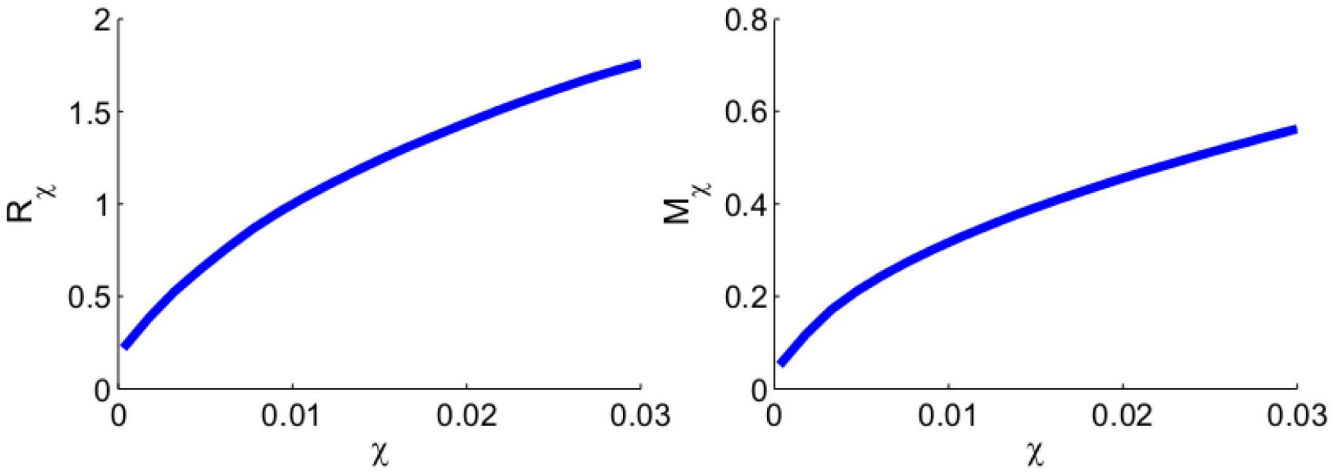

Fig 6. The growth of R_χ and M_χ. (a) The distance that the invasion front traveled by day 60 (R_χ, in unit of cm). (b) The total linear mass of cancer cells at day 60 (M_χ, in unit of g). χ ranges from 3×10^{-4} to 3×10^{-2} $cm^5g^{-1}day^{-1}$. All other parameter values are the same as in the EGFR-mutation case of Fig 3.

doi:10.1371/journal.pone.0167706.g006

ϕ_R is approximately 33% when $\chi = 3 \times 10^{-4}g^{-1}day^{-1}$, and it increases to 40% when $\chi = 3 \times 10^{-4}g^{-1}day^{-1}$. The efficacy ϕ_M is 57% when $\chi = 3 \times 10^{-4}g^{-1}day^{-1}$, and it increases to 68% when $\chi = 3 \times 10^{-4}g^{-1}day^{-1}$.

From Figs 6 and 7 we conclude that as χ increases, the tumor invasion and total mass increase, while at the same time the efficacy of anti-miRs drug also increases. The same results (not shown here) hold for other mutations as well as for the control case.

Fig 8 shows the relationship between the invasion distance in the control case to the total mass of miR-21 and the total mass of miR-155 after the first 60 days. Since the concentration of miRs in serum are positively correlated to their concentration in lung cancer tissue [10–12],

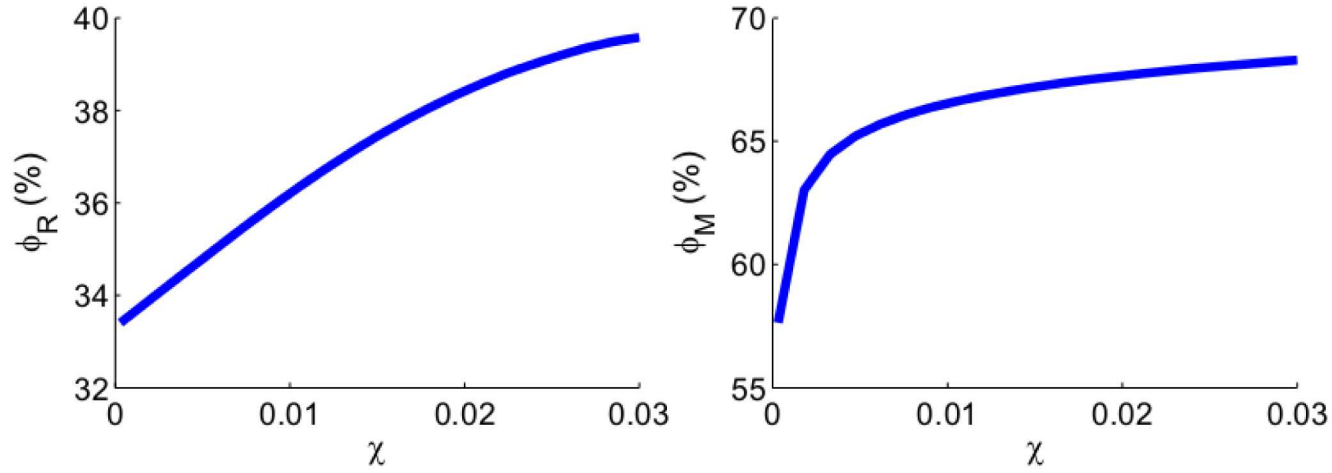

Fig 7. The growth of ϕ_R and ϕ_M. (a) The efficacy (ϕ_R) of anti-miR drugs in reducing the distance traveled by the tumor front at day 60. (b) The efficacy (ϕ_M) of anti-miR drugs in reducing the total linear mass of cancer cells at day 60. χ varies from 3×10^{-4} to 3×10^{-2} $cm^5g^{-1}day^{-1}$. The anti-miR drugs reduce both λ_{m_1} and λ_{m_2} by a factor 2. All other parameter values are the same as Fig 6.

doi:10.1371/journal.pone.0167706.g007

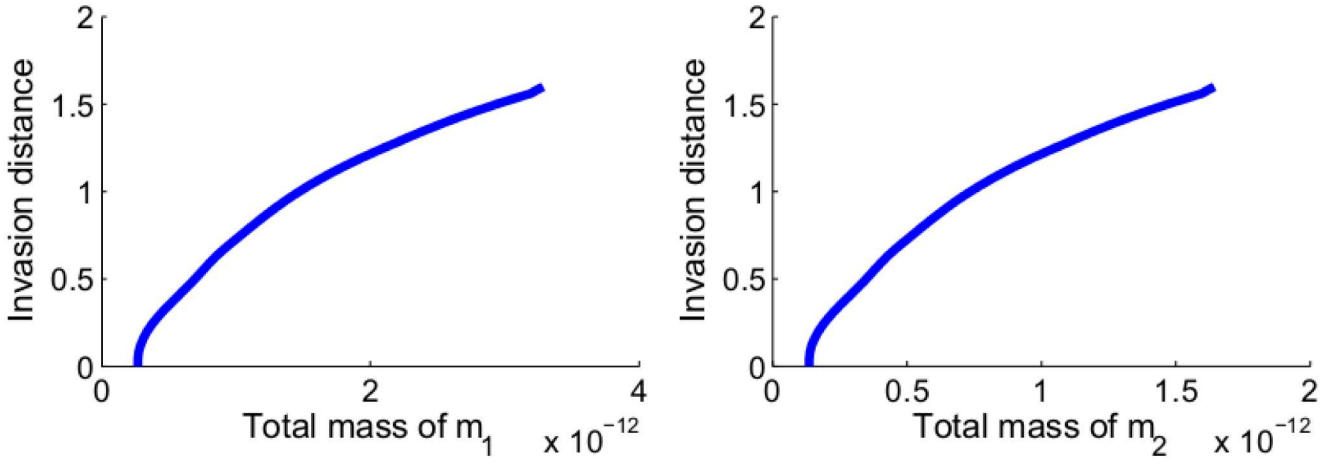

Fig 8. Growth of invasion distance as a function of the total mass of m_1 and total mass of m_2. (a) The invasion distance of cancer cells in the control case as a function of the total mass of miR-21 and miR-205. (b) The invasion distance of cancer cells as a function of the total mass of miR-155. All the parameter values are the same as the control case in Fig 3.

doi:10.1371/journal.pone.0167706.g008

Fig 8 suggests that miR-21 and miR-155 could potentially be used as serum biomarkers for NSCLC, in line with suggestions made in [5, 7].

Results for tumor proliferation

The simulations of proliferation of cancer cells are based on the model Eqs (1)–(8), (16)–(18) with boundary Conditions (19) and initial Conditions (20). We increase both λ_{C1} and λ_{C2} by a factor 1.4 compared to the values in tumor invasion model in order to account for the fact that proliferating cells grow faster than migrating cells [37–39]. We also increase the steady state C_0 from 0.4 g/cm^3 to 0.46 g/cm^3 to reflect the fact that invading cancer cells have sparser density than proliferating cells. We take the steady state density of healthy cells, N_0, to be 0.14 g/cm^3 so that Eq (17) holds. All the other parameter values are the same as in Tables 2 and 3. We take the initial tumor radius to be $R(0) = 0.01$ cm.

Fig 9 shows the average concentrations of all the variables over a period of 60 days. Most of the concentrations are either monotone increasing or monotone decreasing in time: the cell growth inhibitors TKI, PTEN and Apaf-1 are decreasing, while the cell growth promoters are increasing. The only exception is the average density of E. It is initially increasing since MAPK density is small. But MAPK continues to increase (as T keeps decreasing), and after a few days the inhibition by MAPK (or actually ERK, see Fig 1) forces E to decrease, and it does so until it reaches a steady state.

We note that in estimating some of the parameters of the model equations we assumed steady-state of the various variables (cells, proteins, miRs). The steady state of the variables in Fig 9 agree approximately with those steady state values, and this establishes consistency of our assumed steady-state values. In particular, the average density of cancer cells stabilize at 0.4631 g/cm^3, and the average density of normal healthy cells stabilize at 0.1337 g/cm^3, while $C + N$ remains approximately equal to 0.6 g/cm^3 at the entire time.

Fig 10 shows the growth of the tumor radius and volume, and of the total mass of m_1 and m_2 for the first 60 days. From these profiles we can deduce relations between the total volume of the tumor and the total mass of m_1 and of m_2, at day 60. These relations are shown in Fig 11.

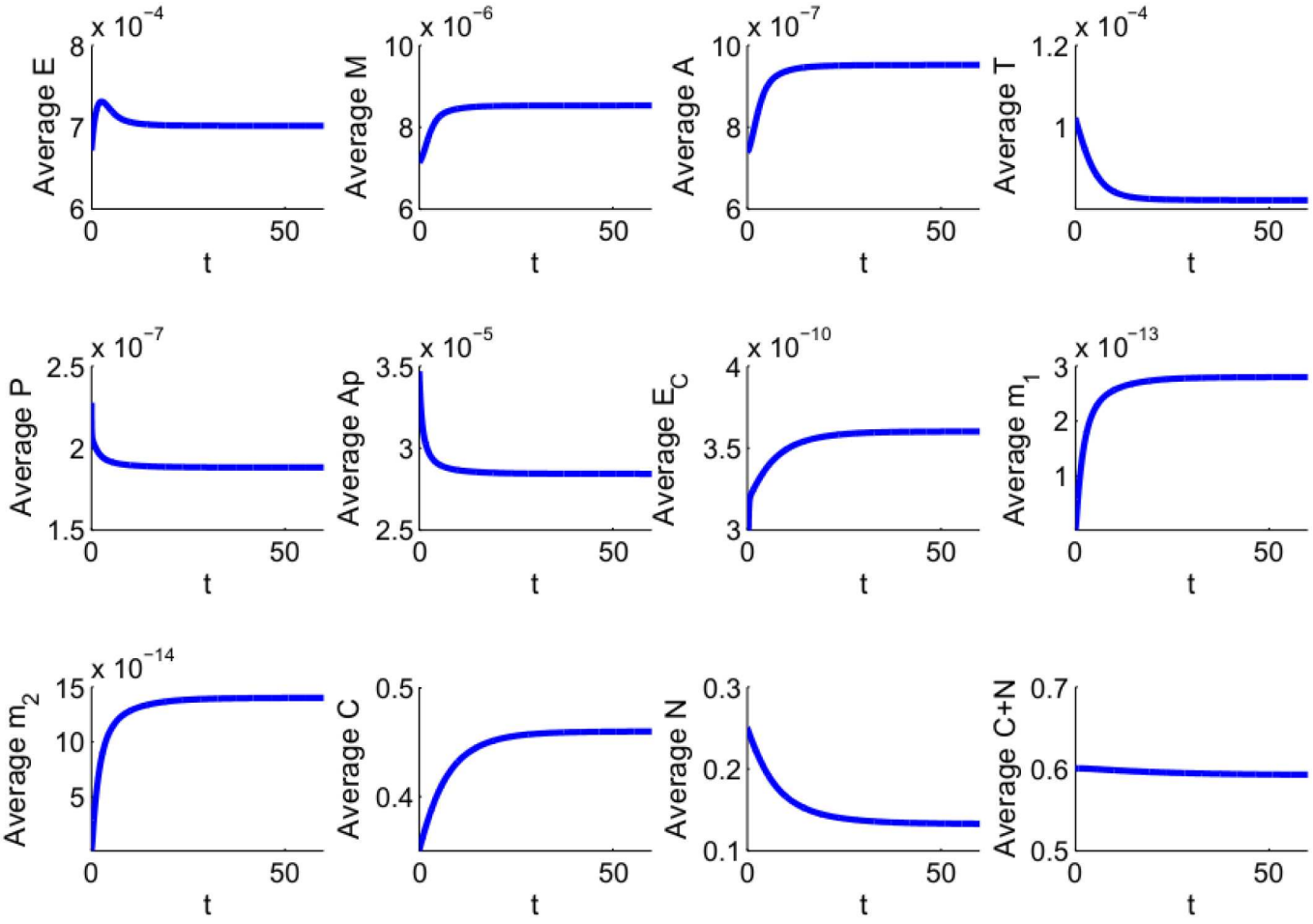

Fig 9. Average densities/concentrations of all the variables in the model. λ_{C1} and λ_{C2} are increased by a factor 1.4. $\theta = 0.6$ g/cm^3, $C_0 = 0.46$ g/cm^3 and $N_0 = 0.14$ g/cm^3. All other parameter values are the same as in Tables 2 and 3.

doi:10.1371/journal.pone.0167706.g009

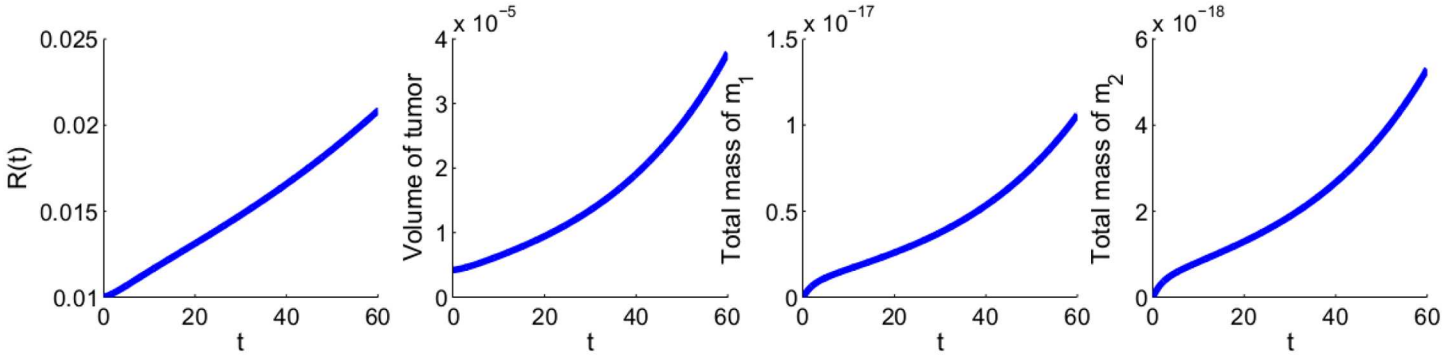

Fig 10. The growth of tumor radius $R(t)$, tumor volume, total mass of m_1 and total mass of m_2 for the first 60 days. λ_{C1} and λ_{C2} are increased by a factor 1.4. θ is taken to be 0.6g/cm^3. All other parameter values are the same as in Tables 2 and 3.

doi:10.1371/journal.pone.0167706.g010

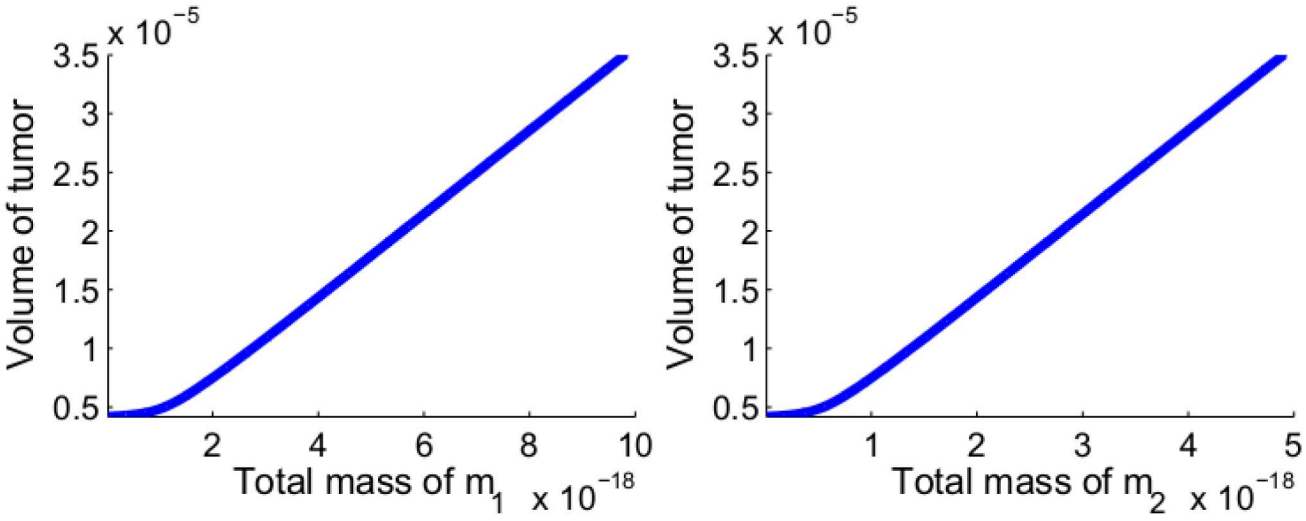

Fig 11. Volume of tumor as a function of the total mass of miR-21 and that of miR-155. (a) The volume of tumor as a function of the total mass of miR-21 after the first 60 days. (b) The volume of tumor as a function of the total mass of miR-155 after the first 60 days. All the parameter values are the same as Fig 10.

doi:10.1371/journal.pone.0167706.g011

Fig 11 may suggest that miR-21 and miR-155 could be used as biomarkers for determining the volume of NSCLC when this volume is still extremely small; however this suggestion is highly speculative at this time, since other miRs shed from both the cancer cells and immune cells are also circulating in the blood.

We note that the corresponding Fig 8 simulates a different situation, where the tumor is already well established in $\{x < 0\}$ and its front begins to invade into $\{x > 0\}$.

Treatment

It is well known that cancer cells in NSCLC lose sensitivity to anti-tumor drugs, for example to paclitaxel, gefitinib and cisplatin, and that some anti-miRs can restore some of this sensitivity. We use our model to explore the effect of anti-miR combined with paclitaxel, gefitinib and cisplatin.

Paclitaxel drugs (PTX) block progression of mitosis by protecting microtubules against disassembly and preventing chromosomes from achieving metaphase spindle configuration [41]. Researches have observed that paclitaxel-treated cells have defects in mitotic spindle assembly, chromosome segregation and cell division [41]. Experiments *in vivo* by Yung et al. [42] show that anti-miR-21 reduces tumor volume in NSCLC, and the combination of paclitaxel and anti-miR-21 demonstrated greater ability to reduce cancer cell proliferation than either agent administered alone. The simulations in Fig 12(a) mimic this experiment; the effect of PTX is accounted for by reducing $1.4\lambda_{Ci}$ to $1.3\lambda_{Ci}$ ($i = 1, 2$), and the effect of anti-miR-21 is accounted for by reducing λ_{m_1} to $\lambda_{m_1}/2$. We note however that in our model the cancer is at an earlier stage and its volume is much smaller compared to the volume of 0.8 cm^3 in [42].

Gefitinib is a drug used in the treatment of NSCLC. It blocks the production of EGF-EGFR and thus obstructs the MAPK and AKT pathways [43]. Tumor cells that are initially sensitive to gefitinib may eventually lose sensitivity due to the emergence of acquired resistance [44]. Alternative mechanisms are currently being explored aimed to overcome the development of gefitinib resistance in the patients of NSCLC [44, 45]. Recent studies [8, 25] show that miR-21

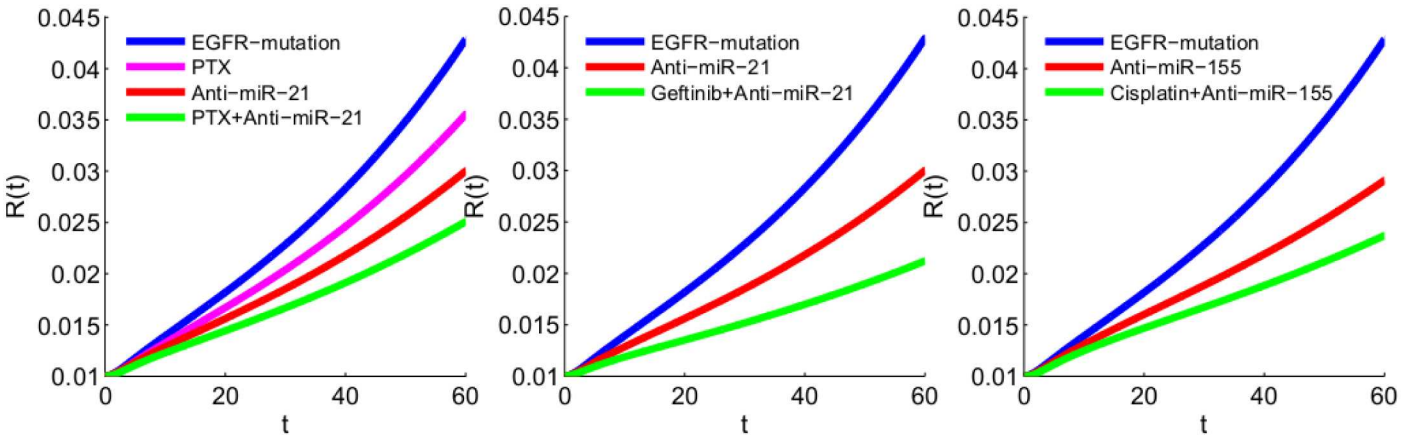

Fig 12. Tumor growth under different drugs. EGFR mutation is accounted for by increasing λ_E by factor 3. (a) Paclitaxel inhibits the division of cells, where λ_{Ci} are reduced from $1.4\lambda_{Ci}$ to $1.3\lambda_{Ci}$ ($i = 1, 2$); anti-miR-21 is accounted for by reducing λ_{m_1} to $\lambda_{m_1}/2$. (b) Both anti-miR-21 and the gefitinib, a drug that inhibits the EGFR, reduce the growth of tumor; anti-miR-21 is accounted for by reducing λ_{m_1} to $\lambda_{m_1}/2$, and EGFR-inhibitor gefitinib is accounted for by decreasing $3\lambda_E$ to $1.5\lambda_E$. (c) Anti-miR-155 is accounted for by reducing λ_{m_2} to $\lambda_{m_2}/1.2$ and cisplatin, a drug that induces cancer cell apoptosis, is accounted for by increasing d_C and d_D by factor 1.1.

doi:10.1371/journal.pone.0167706.g012

modulates gefitinib sensitivity. In particular, Shen et al. [8] demonstrated *in vivo* that reduction in miR-21 significantly restored gefitinib sensitivity by up-regulation of PTEN expression and the inactivation of AKT and MAPK pathways. We can use our model to represent the experimental results of Shen et al. [8]. We account for the effect of gefitinib by reducing $3\lambda_E$, in the case of EGFR mutation, to $1.5\lambda_E$, and the effect of anti-miR-21 by reducing λ_{m_1} to $\lambda_{m_1}/2$. Fig 12 (b) shows that anti-miR-21 alone reduces the growth of tumor volume, but in combination with gefitinib the reduction is significantly larger. This is in qualitative agreement with the results in [8], although here again our model considers an early stage of a tumor whereas, in [8], the tumor volume is already 0.5 cm^3.

Cisplatin induces cancer cell apoptosis by inhibition of DNA synthesis and repair in cell cycle [46]. The efficacy of cisplatin is initially high, but in the majority of cancer patients it eventually drops due to cisplatin resistance. Many mechanisms of cisplatin resistance have been described, including changes in cellular uptake, drug efflux, increased detoxification of the drug, inhibition of apoptosis, and increased DNA repair [46]. Experiments by Zang et al. [30] show that down-regulation of miR-155 can enhance the sensitivity of lung cancer cells to cisplatin treatment through the induction of DNA damage and apoptosis via the restoration of the mitochondrial apoptotic pathway. The simulation in Fig 12(c) shows that anti-miR-155 alone reduces the tumor volume, but in combination with cisplatin the reduction is significantly higher.

Discussion and conclusion

Worldwide, lung cancer is the leading cause of cancer deaths, and approximately 85% of lung cancer cases are NSCLC [1, 2]. Five years survival rate for NSCLC is significantly higher for those diagnosed at early stage [3]. Unlike mammography for breast cancer or colonoscopy for colon cancer there are no reliable tools for early detection of lung cancer; most lung cancers are first diagnosed on symptoms. Hence, there is increased focus on identifying biomarkers for detection of NSCLC at early stage [5].

A growing body of evidence suggests that exosomal miRs may be used as serum biomarkers for prognosis of malignant tumors [5, 7]. In NSCLC the highest overexpressed miRs are miR-21, miR-205 and miR-155 [6, 10]. Since exosomal miRs concentration in the blood are positively correlated to their concentrations in tissue [10–12], it is important to understand how the concentrations of miRs 21, 205 and 155 in NSCLC tissue are related to the progression of the cancer, both in terms of tumor growth and tumor-front invasion.

In the present paper we developed a mathematical model that relates the role of the above exosomal miRs in tissue to cancer cells proliferation and invasion. MiRs 21 and 205 regulate cell proliferation through MAPK and PI3K-AKT pathways, while miR-155 regulates apoptosis through the Apaf-1-Caspase 9 complex. The mathematical model includes, separately, invasion and proliferation phases of NSCLC. In invasion, the 'directed migration coefficient' χ plays a critical role: the tumor front increases as χ increases. In order to visualize this monotonic relation, we used a 'relatively' large χ; *in vivo* this parameter may be much smaller.

In the model of tumor proliferation, what makes the tumor volume grow is the fact that the combined densities of cancer cells (C) and healthy cells (N) is limited, i.e, $C + N$ = constant. Simulations of the proliferating model show qualitative agreement with experimental results in the treatment of NSCLC. In these experiments, miR-21 and miR-155 are used to re-establish sensitivity of cancer cells to specific chemotherapeutic drugs.

Simulations of the model of tumor proliferation establish quantitative relations between the total mass of over-expressed miRs (21, 205, 155) and tumor volume. Because of the positive correlation between miRs in cancer tissue and serum [10–12], the present model may be viewed as a first step toward establishing a combination of miRs 21, 205, 155 and possibly additional miRs as serum biomarkers for early detection of NSCLC. As more experimental and clinical data become available, the model could then be refined by estimating more precisely some of the parameters, by expanding the genetic network of Fig 2, and by precisely relating the concentrations of miRs in serum to miRs in lung tissue.

Parameter values

In the sequal we shall use the following conversion of units: 1Da = 1g/mol, so that

$$1 \text{ mol of a protein with molecular weight } m\text{kDa has a mass of } m \times 10^3\text{g}. \quad (21)$$

Also, 1 Molar = 1 mol/L = 10^{-3}mol/cm^3. Hence 1nM = 10^{-12} mol/cm^3, and

$$\text{Concentration of 1nM of a protein with molecular weight } m\text{kDa} = m \times 10^{-9}\ \text{g/cm}^3. \quad (22)$$

Steady state concentrations

In some estimating parameters, we use steady state equations; we denote the steady state concentrations of species X by X_0.

EGF-EGFR Cancer cells express $2 - 3 \times 10^6$ EGFR proteins per cell [47]. We take the average to be 2.5×10^6 EGFR per cell, or $\frac{2.5\times10^6}{N_A}$ fraction of a mole, per cell, where $N_A = 6.022 \times 10^{23}$ is Avogadro's number. The molecular weight of EGFR is 170kDa [47]. By Eq (21), the mass of EGFR in one cell is $\frac{2.5\times10^6}{N_A} \times 170 \times 10^3\text{g} = 7.0573 \times 10^{-13}$g. Assuming that one cell has a volume of 10^{-9}cm^3, we find that the concentration of EGFR is 7.0573×10^{-4} g/cm^3. We assume that the concentration of EGF-EGFR is not limited by the availability of EGF, hence $E_0 = 7.0573 \times 10^{-4}$g/cm^3.

MAPK The molar concentration of Ras is 0.4μM [48] and its molecular weight is 21kDa [49]. Hence, by Eq (22), the concentration of Ras is $M_{01} = (0.4 \times 10^3) \times 21 \times 10^{-9}$g/cm^3 =

8.4×10^{-6}g/cm^3. The molar concentration of Raf is 0.013μM [48, 50], and its molecular weight is 72kDa [48]. Hence the concentration of Raf is $M_{02} = (0.013 \times 10^3) \times 72 \times 10^{-9}$g/cm^3 = 0.936×10^{-6}g/cm^3. The molar concentration of MEK is 1.4μM [48, 49] and its molecular weight is 43kDa [51]. Hence the concentration of MEK is $M_{03} = (1.4 \times 10^3) \times 43 \times 10^{-9}$g/cm^3 = 6.02×10^{-5}g/cm^3. The molar concentration of ERK is 0.96μM [48, 49] and its molecular weight is 41kDa [52]. Hence the concentration of MEK is $M_{04} = (0.96 \times 10^3) \times 41 \times 10^{-9}$g/cm^3 = 3.936×10^{-5}g/cm^3. All the M_{0i} are of the same order of magnitude. In estimating parameters, we shall use the steady state concentration M_0 of the MAPK. We take it to be that of Ras, that is $M_0 = M_{01}$, since steady state of Ras leads to steady state in the MAPK pathway.

PI3K The molar concentration of PI3K is 8nM [53, 54], and its molecular weight is 195kDa [55]. Hence, by Eq (22), the concentration of PI3K is $P_{30} = 8 \times 195 \times 10^{-9}$g/cm^3 = 1.56×10^{-6}g/cm^3.

AKT The molar concentration of AKT is 15.1nM [47], and its molecular weight is 62kDa [47]. Hence, by Eq (22), the concentration of AKT is given by $A_0 = 15.1 \times 62 \times 10^{-9}$g/cm^3 = 9.362×10^{-7}g/cm^3.

PTEN The molar concentration of PTEN is 4nM [56], and its molecular weight is 47kDa [56]. Hence, by Eq (22), the concentration of PTEN is $P_0 = 4 \times 47 \times 10^{-9}$g/cm^3 = 1.88×10^{-7}g/cm^3.

TKI TKI inhibits the activation of PI3K, and PTEN inhibits the activation of AKT. We assume that these two inhibitions are proportional, that is $T_0/E_0 = P_0/P_{30}$. Hence $T_0 = P_0E_0/P_{30}$ = 8.5050×10^{-5}g/cm^3.

Apaf-1 The molar concentration of Apaf-1 ranges from 0.1μM to 0.5μM [57]. We take it to be 0.2μM. The molecular weight of Apaf-1 is 142kDa [57]. Hence, by Eq (22), the concentration of Apaf-1 is $(0.2 \times 10^3) \times 142 \times 10^{-9}$g/cm^3 = 2.84×10^{-5}g/cm^3. We assume that the concentration of Apaf-1-caspase-9 apoptosome is not limited by the availability of caspase 9, hence the concentration is $A_{p0} = 2.84 \times 10^{-5}$g/cm^3.

Exosome In breast cancer, 10^6 cancer cells release 5×10^8 exosomes in 24 hours [58]. Assuming that the number of cancer cells in lung cancer is 4×10^8 per cm^3, and taking the average diameter of exosomes to be 70nm, we estimate the mass density of E_C by E_{C0} = 3.6×10^{-10}g/cm^3.

MiR-21, miR-205 and miR-155 For simplicity, we assume steady state of Eqs (10) and (11), so that $m_1^i = m_{10}^i, \quad m_2^i = m_{20}^i$. We also assume that the cellular concentration of miR-21 is proportional to the exosomal concentration of miR-21, in the sense that $m_{10}^i = \gamma m_{10}$, where m_{10} is the steady state of m_1. Similarly, we assume $m_{20}^i = \gamma m_{20}$, where m_{20} is the steady state of m_2. In the simulations, we take $\gamma = 10$, but the simulations do not change qualitatively if we use different values of γ of the same order of magnitude.

The range of molar concentration of miR-21 in healthy individuals is 0.1-0.326 amol/μL [59, 60], and we take it to be 0.2 amol/μL, that is $\frac{0.2\times10^{-18}}{10^{-3}}$mol/cm^3 = 0.2×10^{-3}nM. The molecular weight of miR-21 is 7kDa [61]. Hence, by Eq (22), the cellular concentration of miR-21 is $(0.2 \times 10^{-3}) \times 7 \times 10^{-9}$g/cm^3 = 1.4×10^{-12}g/cm^3. The concentrations of miR-205 and miR-155 are approximately the same as concentration of miR-21 [10]. Since in our model we combine miR-21 and miR-205, we take $m_{20}^i = 1.4 \times 10^{-12}$g/cm^3, while $m_{10}^i = 2.8 \times 10^{-12}$g/cm^3. Hence, $m_{20} = 1.4 \times 10^{-13}$g/cm^3 and $m_{10} = 2.8 \times 10^{-13}$g/cm^3.

NSCLC We take, for the invasion model, $C_M = 0.8$g/cm^3 and $C_0 = 0.4$g/cm^3 [62].

Parameter estimation

In the sequal, in expressions of enhancement of the form $\frac{X}{K+X}$ or inhibition of the form $\frac{1}{1+X/K}$, the parameter K, the 'half-saturation' of X, will be taken to be the steady state of X. Thus K_{MA} =

$K_M = M_0$, $K_A = A_0$, $K_{Ap} = A_{p0}$ and $K_C = C_0$, and $K_{ME} = M_0$, $K_{TM} = K_{TA} = T_0$, $K_{PA} = P_0$. However, we make an exception in the case of miRs; we assume that the inhibition of protein expressions by miRs is more significant than inhibition by signaling proteins, and take $K_{mT} = m_{10}/5$, $K_{mP} = m_{10}/5$ and $K_{m_2} = m_{20}/5$.

For a species with concentration X and half-life $t_{1/2}$, the dynamics of its degradation or death is given by

$$\frac{dX}{dt} = -d_X X, \quad \text{where} \quad d_X = \ln 2/t_{1/2}.$$

Parameter estimation for Eq (1): The half-life of EGFR ranges from 8 to 24 hours [47]. We take it to be 20 hours, i.e. $t_{1/2} = 5/6$ days, so that $d_E = \ln 2/t_{1/2} = 0.8318$ days^{-1}. From the steady state of Eq (1) with $K_{ME} = M_0$, we deduce that $\lambda_E = 2d_E E_0 = 1.1741 \times 10^{-3}$day^{-1} · g/cm^3.

Parameter estimation for Eq (2): The half-life of KRAS is 12 hours [63]; the half-life of Raf is 30 hours [64]; the half-life of MEK is 8 hours [65], and the half-life of ERK is 24 hours [66]. We take the half-life of the combined pathway MAPK to be 24 hours, that is $t_{1/2} = 1$ day, then $d_M = 0.6931$ day^{-1}. From the the steady state of Eq (2) with $K_{TM} = T_0$, we find that $\lambda_M = 2d_M M_0/E_0 = 1.6499 \times 10^{-2}$day^{-1}.

Parameter estimation for Eq (3): The half-life of AKT ranges from 12 to 36 hours [67, 68]. We take it to be 24 hours, that is, $t_{1/2} = 1$ day, so that $d_A = 0.6931$day^{-1}. We assume that the activation of AKT pathway by Ras is weaker than the activation by EGF-EGFR, and take $\lambda_{MA} = 1/2$. From the steady state of Eq (3) with $K_{TA} = T_0$, $K_{PA} = P_0$ and $K_{MA} = M_0$, we find that $\lambda_A = (16/5) \cdot d_A A_0/E_0 = 2.9422 \times 10^{-3}$day^{-1}.

Parameter estimation for Eq (4): The half-life of the TKI drugs erlotinib, ASD9291 and sunitinib are 36, 50 and 40-60 hours [69]. We take the half-life of TKI to be 48 hours, that is, $t_{1/2} = 2$ days. Hence $d_T = 0.3466$ day^{-1}. From the steady state equation of Eq (4) with $K_{mT} = m_{10}/5$, we find that $\lambda_T = 28.5 d_T T_0 = 8.4013 \times 10^{-4}$day^{-1} · g/cm^3.

Parameter estimation for Eq (5): The half-life of PTEN is 45 minutes [70, 71], that is $t_{1/2} = 0.03125$ days, so that $d_P = 22.1807$ day^{-1}. From the steady state of Eq (5) with $K_{mP} = m_{10}/5$, we find that $\lambda_P = 56 d_P P_0 = 2.3352 \times 10^{-4}$day^{-1} · g/cm^{-3}.

Parameter estimation for Eq (6): The half-life of Apaf-1 is 1.81h [72]; the half-life of caspase-9 is 6.6h [73]. We assume that Apaf-1-caspase-9 apoptosome is as stable as caspase-9, and take the half-life of the apoptosome to be 6h, that is $t_{1/2} = 0.25$ days. Then $d_{Ap} = 2.7726$ day^{-1}. From the steady state of Eq (6) with $K_{m_2} = m_{20}/5$, we get $\lambda_{Ap} = 56 d_{Ap} Ap_0 = 4.4095 \times 10^{-3}$ day^{-1} · g/cm^3.

Parameter estimation for Eq (7): The rate of breakdown of exosomes upon contact with cancer cells is unknown. We take this rate to be $d_{Ec} = 21.8$ day^{-1}. From the steady state of Eq (7) with $K_C = C_0$, we get $\lambda_{Ec} = d_{Ec} E_{C0}/(2C_0) = 9.81 \times 10^{-9}$ day^{-1}.

Parameter estimation for Eq (8): The half-life of miRs is greater than 24 hours [74]; we take half-life of miR-21 to be 30 hours, i.e. $t_{1/2} = 1.25$ day. Hence $d_{m_1} = 0.5545$ day^{-1}. From the steady state of Eq (8) with $K_C = C_0$, we get $\lambda_{m_1} = 2d_{m_1} m_{10}/E_{C0} = 0.8626 \times 10^{-3}$ day^{-1}.

Parameter estimation for Eq (9): We take the half-life of miR-155 to be 30 hours [74], and then $d_{m_2} = 0.5545$ day^{-1}. From the steady state of Eq (9) with $K_C = C_0$, we obtain $\lambda_{m_2} = 2d_{m_2} m_{20}/E_{C0} = 0.4313 \times 10^{-3}$day^{-1}.

Parameter estimation for Eq (12): The most common mutations in NSCLC occur in tumor suppressors TP53 and ALK, and in oncogenes PTEN, EGFR, KRAS, LKB1 and BRAF, and mutations seem to occur more frequently in MAPK (KRAS, BRAF) than in PI3K-AKT [21, 75, 76]. We accordingly assume that the proliferation rate of cancer cells through the MAPK pathway is higher than the proliferation rate through the AKT pathway, and take $\lambda_{C1} =$

$2\lambda_{C2}$. We also assume that in steady state

$$\frac{1}{2}\lambda_{C1} + \frac{1}{2}\lambda_{C2} = \lambda_C,$$

and take $\lambda_C = 0.46$ day^{-1} [77]. Hence $\lambda_{C1} = (4/3)\lambda_C = 0.6133$ day^{-1} and $\lambda_{C2} = (2/3)\lambda_C = 0.3067$ day^{-1}.

From the steady state equation of Eq (12) with $K_M = M_0$, $K_A = A_0$, $K_{Ap} = Ap_0$ and $C_0 = C_M/2$, we get

$$\frac{1}{2}d_D + d_C = \frac{1}{2}\lambda_C, \quad \text{or} \quad d_D + 2d_C = \lambda_C.$$

We assume that apoptosis rate through intrinsic apoptosis pathway (Apaf-1/Caspace-9) is higher than apoptosis through the extrinsic signaling pathway [78], and take d_D to be larger than d_C, so that $d_D = 0.9\lambda_C$ and $2d_C = 0.1\lambda_C$. Hence $d_D = 0.414$ and $d_C = 0.023$.

Diffusion coefficients: We take $D_C = 8.64 \times 10^{-7}$cm^{2}day^{-1} [77]. Diffusion of a sphere is inversely proportional to its diameter. We assume that the average diameter of exosome and cells are 70nm and 10μm respectively. Then we get $D_{E_C} = \frac{8.6\times10^{-7}}{7\times10^{-3}} = 1.23 \times 10^{-4}$ cm^2 day^{-1}. By [79], we have the relation $D_{m_1} = \frac{M_V^{1/3}}{M_{m_1}^{1/3}} D_V$, where D_V and M_V are the diffusion coefficient and molecular weight of vascular endothelial growth factor (VEGF), respectively, and $D_V = 8.64 \times 10^{-2}$ [77], and $M_V = 24kDa$ [80]. The molecular weight of miR-21 is $M_{m_1} = 7$ kDa, hence $D_{m_1} = 0.13028$ cm^{2}day^{-1}, and similarly $D_{m_2} = 0.13028$ cm^{2}day^{-1}. The directed migration coefficient χ is taken to be in the range $3 \times 10^{-4} - 3 \times 10^{-2}$ cm^{5}g^{-1}day^{-1} [33]. In cell invasion, χ should be much larger than in cell growth, so we take $\chi = 2 \times 10^{-2}$ cm^{5}g^{-1}day^{-1} for the model of tumor invasion.

Parameter estimation for Eq (16): Cancer cells can survive in hostile environment better than normal cells, so the apoptosis rate d_N should be somewhat larger than d_C; we take $d_N = 1.1d_C = 0.0253$ day^{-1} and $\lambda_N = 0.8\lambda_C = 0.368$ day^{-1}. Since cancer cells replication is less susceptible to damage, d_{DN} should be larger than d_D; we take $d_{DN} = 1.1d_D = 0.4554$ day^{-1}. We choose $\varepsilon = 0.1$, as in [40]. We assume that C_0 in the proliferation phase to be somewhat larger than the average density 0.4 g/cm^3 in the invasion phase; we take $C_0 = 0.46$ g/cm^3 and $N_0 = 0.14$ g/cm^3.

Sensitivity analysis

We performed sensitivity analysis on some of the production parameters of the system Eqs (1)–(9), (15)–(18); we also included the important parameter d_{Ec} which was only fitted. Following the method of [81] we performed Latin hypercube sampling and generated 1000 samples to calculate the partial rank correlation coefficients (PRCC) and the p-values with respect to the tumor radius at day 60. We have taken the range of each parameter from 1/2 to twice its value in Table 2. The results are shown in Fig 13.

We see that the production rates that increase proliferation through EGF-EGFR → MAPK and EGF-EGFR → AKT pathways, namely, (λ_E, λ_M) and (λ_E, λ_M, λ_{MA}) are positively correlated to tumor radius. On the other hand the production rates of cell-replication inhibitors, λ_T and λ_P, and the production rate of apoptosis-promotor apoptosome, λ_{Ap}, are negatively correlated. Since miR-21 blocks the inhibitors T and P, so if $\lambda_{m_1}E_C$ grows the tumor volume will increase. Hence λ_{m_1} is positively correlated and d_{Ec} is negatively correlated.

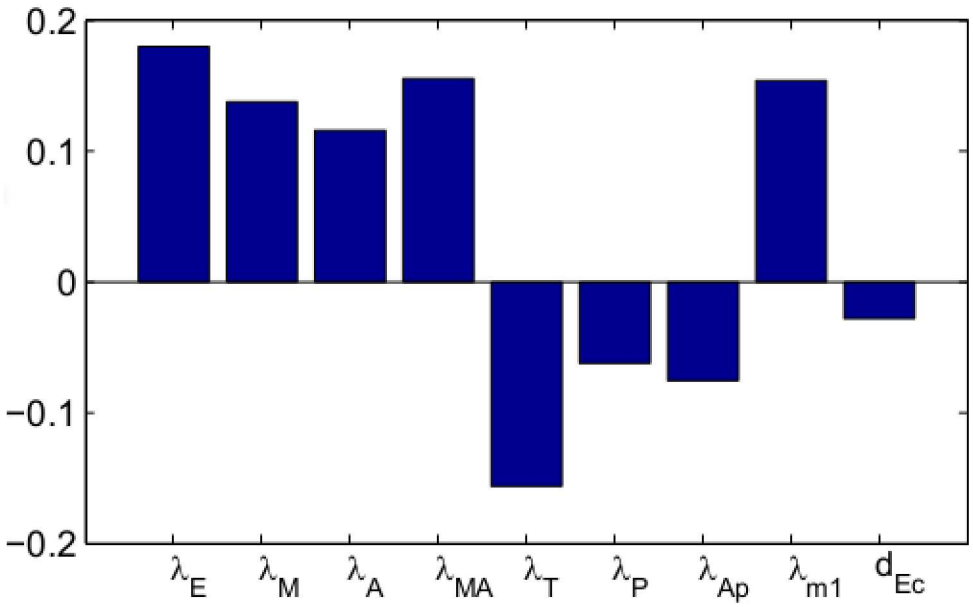

Fig 13. Statistically significant PRCC values (p-value < 0.01) for *R*(*t*) at day 60.

doi:10.1371/journal.pone.0167706.g013

Computational method

We employ moving mesh method to numerically solve the free boundary problem for the tumor proliferation model. To illustrate this method, we take Eq (16) as example and rewrite it as the following form:

$$\frac{\partial N(r,t)}{\partial t} = D_N \Delta N(r,t) - div(\mathbf{u}N) + F, \tag{23}$$

where F represents the term in the right hand side of Eq (16). Let r_i^k and N_i^k denote numerical approximations of i-th grid point and $N(r_i^k, n\tau)$, respectively, where τ is the size of time-step. The discretization of Eq (23) is derived by the fully implicit finite difference scheme:

$$\frac{N_i^{k+1} - N_i^k}{\tau} = D_N\left(N_{rr} + \frac{N_r}{r_i^k}\right) - \left(\frac{u_r}{r_i^{k+1}} + u_i^{k+1}\right)N_i^{k+1} + F_i^{k+1}, \tag{24}$$

where $N_r = \frac{h_{-1}^2 N_{i+1}^{k+1} - h_1^2 N_{i-1}^{k+1} - (h_1^2 - h_{-1}^2)N_i^{k+1}}{h_1(h_{-1}^2 - h_1 h_{-1})}$, $N_{rr} = 2\frac{h_{-1}N_{i+1}^{k+1} - h_1 N_{i-1}^{k+1} + (h_1 - h_{-1})N_i^{k+1}}{h_1(h_1 h_{-1} - h_{-1}^2)}$),
$u_r = \frac{h_{-1}^2 u_{i+1}^{k+1} - h_1^2 u_{i-1}^{k+1} - (h_1^2 - h_{-1}^2)u_i^{k+1}}{h_1(h_{-1}^2 - h_1 h_{-1})}$, $h_{-1} = r_{i-1}^{k+1} - r_i^{k+1}$ and $h_1 = r_{i+1}^{k+1} - r_i^{k+1}$. The mesh moves by $r_i^{k+1} = r_i^k + u_i^{k+1}\tau$, where u_i^{k+1} is solved by the velocity equation.

Acknowledgments

This work is supported by the Mathematical Biosciences Institute and the National Science Foundation (Grant DMS 0931642), the National Natural Science Foundation of China (Grant No. 11501568), and the Fundamental Research Funds for the Central Universities and the Research Funds of Renmin University of China.

Author Contributions

Conceptualization: AF XL.

Data curation: AF XL.

Formal analysis: AF XL.

Funding acquisition: AF XL.

Investigation: AF XL.

Methodology: AF XL.

Project administration: AF.

Resources: AF XL.

Software: AF XL.

Validation: AF XL.

Writing – original draft: AF XL.

Writing – review & editing: AF XL.

References

1. Siegel RL, Miller KD, Jemal A. Cancer Statistics 2015. CA CANCER J CLIN. 2015; 65:5–29. doi: 10.3322/caac.21254 PMID: 25559415
2. Ferlay J, Soerjomataram I, Dikshit R, Eser S, Mathers C, Rebelo M, et al. Cancer incidence and mortality worldwide: sources, methods and major patterns in GLOBOCAN 2012. Int J Cancer. 2015; 136(5): E359–86. doi: 10.1002/ijc.29210 PMID: 25220842
3. Henschke CI, McCauley DI, Yankelevitz DF, Naidich DP, McGuinness G, Miettinen OS, et al. Early Lung Cancer Action Project: overall design and findings from baseline screening. Lancet. 1999; 354 (9173):99–105. doi: 10.1016/S0140-6736(99)06093-6 PMID: 10408484
4. Ali A, Goffin JR, Arnold A, Ellis PM. Survival of patients with non-small-cell lung cancer after a diagnosis of brain metastases. Curr Oncol. 2013; 20(4):300–6. doi: 10.3747/co.20.1481 PMID: 23904768
5. An T, Qin S, Xu Y, Tang Y, Huang Y, Situ B, et al. Exosomes serve as tumour markers for personalized diagnostics owing to their important role in cancer metastasis. J Extracell Vesicles. 2015; 4:27522. doi: 10.3402/jev.v4.27522 PMID: 26095380
6. Frydrychowicz M, Kolecka-Bednarczyk A, Madejczyk M, Yasar S, Dworacki G. Exosomes-structure, biogenesis and biological role in non-small-cell lung cancer. Scand J Immunol. 2015; 81(1):2–10. doi: 10.1111/sji.12247 PMID: 25359529
7. Properzi F, Logozzi M, Fais S. Exosomes: the future of biomarkers in medicine. Biomark Med. 2013; 7 (5):769–778. doi: 10.2217/bmm.13.63 PMID: 24044569
8. Shen H, Zhu F, Liu J, Xu T, Pei D, Wang R, et al. Alteration in Mir-21/PTEN expression modulates gefitinib resistance in non-small cell lung cancer. PLoS One. 2014; 9(7):e103305. doi: 10.1371/journal.pone.0103305 PMID: 25058005
9. Lei L, Huang Y, Gong W. MiR-205 promotes the growth, metastasis and chemoresistance of NSCLC cells by targeting PTEN. Oncol Rep. 2013; 30(6):2897–902. PMID: 24084898
10. Rabinowits G, Gerçel-Taylor C, Day J, Taylor D, Kloecker G. Exosomal MicroRNA: a diagnostic marker for lung cancer. Clin Lung Cancer. 2009; 10(1):42–46. doi: 10.3816/CLC.2009.n.006 PMID: 19289371
11. Zhao W, Zhao JJ, Hang L, Xu QF, Zhao YM, Shi XY, et al. Serum miR-21 level: a potential diagnostic and prognostic biomarker for non-small cell lung cancer. Int J Clin Exp Med. 2015; 8(9):14759–63. PMID: 26628958
12. Liu R, Liao J, Yang M, Shi Y, Peng Y, Wang Y, et al. Circulating miR-155 expression in plasma: a potential biomarker for early diagnosis of esophageal cancer in humans. J Toxicol Environ Health A. 2012; 75 (18):1154–62. doi: 10.1080/15287394.2012.699856 PMID: 22891887
13. Roberts PJ, Der CJ. Targeting the Raf-MEK-ERK mitogen-activated protein kinase cascade for the treatment of cancer. Oncogene. 2007; 26:3291–3310. doi: 10.1038/sj.onc.1210422 PMID: 17496923

14. Dhillon AS, Hagan S, Rath O, Kolch W. MAP kinase signalling pathways in cancer. Oncogene. 2007; 26:3279–3290. doi: 10.1038/sj.onc.1210421 PMID: 17496922

15. Yip PY. Phosphatidylinositol 3-kinase-AKT-mammalian target of rapamycin (PI3K-Akt-mTOR) signaling pathway in non-small cell lung cancer. Transl Lung Cancer Res. 2015; 4(2):165–176. doi: 10.3978/j.issn.2218-6751.2015.01.04 PMID: 25870799

16. Fumarola C, Bonelli MA, Petronini PG, Alfieri RR. Targeting PI3K/AKT/mTOR pathway in non small cell lung cancer. Biochemical Phamacology. 2014; 90:197–207. doi: 10.1016/j.bcp.2014.05.011 PMID: 24863259

17. Papadimitrakopoulou V, Adjei A. The Akt/mTOR and mitogen-activated protein kinase pathways in lung cancer therapy. J Thoracic Oncology. 2006; 1(7):749–751. doi: 10.1016/S1556-0864(15)30399-3 PMID: 17409953

18. Normanno N, De Luca A, Binanco C, Strizziand L, Mancino M, et al. Epidermal growth factor receptor (EGFR) signaling in cancer. Gene. 2006; 366:2–16. doi: 10.1016/j.gene.2005.10.018 PMID: 16377102

19. Marinov M, Fischer B, Arcaro A. Targeting mTOR signaling in lung cancer. Critical Review in Oncology/Hematology. 2007; 63:172–182. doi: 10.1016/j.critrevonc.2007.04.002 PMID: 17540577

20. Shaw RJ, Cantley LC. Ras, PI(3)K and mTOR signalling controls tumour cell growth. Nature. 2006; 441:424–430. doi: 10.1038/nature04869 PMID: 16724053

21. Siegelin MD, Borczuk AC. Epidermal growth factor receptor mutations in lung adenocarcinoma. Laboratory Investigation. 2014; 94:129–137. doi: 10.1038/labinvest.2013.147 PMID: 24378644

22. Mendoza MC, Er EE, Blenis J. The Ras-ERK and PI3K-mTOR pathways: cross-talk and compensation. Trends Biochem Sci. 2011; 36(6):320–328. doi: 10.1016/j.tibs.2011.03.006 PMID: 21531565

23. Kang HW, Crawford M, Fabbri M, Nuovo G, Garofalo M. A mathematical model for MicroRNA in lung cancer. PLoS ONE. 2013; 8(1):e53663. doi: 10.1371/journal.pone.0053663 PMID: 23365639

24. Sgambato A, Casaluce F, Maione P, Rossi A, Rossi E, Napolitano A, et al. The role of EGFR tyrosine kinase inhibitors in the first-line treatment of advanced non small cell lung cancer patients harboring EGFR mutation. Curr Med Chem. 2012; 19(20):3337–52. PMID: 22664249

25. Li B, Ren S, Li X, Wang Y, Garfield D, Zhou S, et al. MiR-21 overexpression is associated with acquired ressistance of EGFR-TKI in non-small cell lung cancer. Lung cancer. 2014; 83:146–153. doi: 10.1016/j.lungcan.2013.11.003 PMID: 24331411

26. Soengas MS, Alarcon RM, Yoshida H, Giaccia AJ, Hakem R. Apaf-1 and caspase-9 in p53-dependent apoptosis and tumor inhibition. Science. 1999; 284:156–159. doi: 10.1126/science.284.5411.156 PMID: 10102818

27. Bratton SB, Salvesen GS. Regulation of the Apaf-1-caspase-9 apoptosome. J Cell Science. 2010; 123:3209–314. doi: 10.1242/jcs.073643 PMID: 20844150

28. Zhang JG, Wang JJ, Zhao F, Liu Q, Jiang K, Yang GH. MicroRNA-21(miR-21) represses tumor supressor PTEN and promotes growth and invasion in non-small cell lung cancer (NSCLC). Clin Chim Acta. 2010; 411:846–852. doi: 10.1016/j.cca.2010.02.074 PMID: 20223231

29. Zhang G, Hou X, Li Y, Zhao M. MiR-205 inhibits cell apoptosis by targeting phosphatase and tensin homolog deleted on chromosome ten in endometrial cancer ishikawa cells. MBC Cancer. 2014; 14:440. doi: 10.1186/1471-2407-14-440 PMID: 24929707

30. Zang YS, Zhong YS, Fang Z, Li B, An J. MiR-155 inhibits the sensitivity of lung cancer cells to cisplatin via negative regulation of Apaf-1 expression. Cancer Gene Therapy. 2012; 19:773–778. doi: 10.1038/cgt.2012.60 PMID: 22996741

31. Hatley ME, Patrick DM, Garcia MR, Richardson JA, Bassel-Duby R, van Rooij E, et al. Modulation of K-Ras-dependent lung tumorigenesis by MicroRNA-21. Cancer Cell. 2010; 18(3):282–93. doi: 10.1016/j.ccr.2010.08.013 PMID: 20832755

32. Yang Y, Meng H, Peng Q, Yang X, Gan R, et al. Downregulation of microRNA-21 expression restrains non-small cell lung cancer cell proliferation and migration through upregulation of programmed cell death 4. Cancer Gene Ther. 2015; 22(1):23–9. doi: 10.1038/cgt.2014.66 PMID: 25477028

33. Kim Y, Roh S, Lawler S, Friedman A. MiR451 and AMPK mutual antagonism in glioma cell migration and proliferation: a mathematical model. PLoS One. 2011; 6(12):e28293. doi: 10.1371/journal.pone.0028293 PMID: 22205943

34. Salamon R, Backer J. PIP3: Tool of Choice for the Class I PI 3-kinases. Bioessays. 2013; 35(7):602–11. doi: 10.1002/bies.201200176 PMID: 23765576

35. Quaranta V, Rejniak KA, Gerlee P, Anderson AR. Invasion emerges from cancer cell adaptation to competitive microenvironments: quantitative predictions from multiscale mathematical models. Semin Cancer Biol. 2008; 18(5):338–48. doi: 10.1016/j.semcancer.2008.03.018 PMID: 18524624

36. Kam Y, Rejniak KA, Anderson AR. Cellular modeling of cancer invasion: integration of in silico and in vitro approaches. J Cell Physiol. 2012; 227(2):431–8. doi: 10.1002/jcp.22766 PMID: 21465465

37. aand Qian Xie CFG, Su YL, Koeman J, Khoo SK, Gustafson M, et al. Proliferation and invasion: Plasticity in tumor cells. PNAS. 2005; 102(30):10528–10533. doi: 10.1073/pnas.0504367102

38. Matus DQ, Lohmer LL, Kelley LC, Schindler AJ, Kohrman AQ, et al. Invasive cell fate requires G1 cell-cycle arrest and Histone Deacetylase-mediated changes in gene expression. Developmental Cell. 2015; 35(2):162–174. doi: 10.1016/j.devcel.2015.10.002 PMID: 26506306

39. Gil-Henn H, Patsialou A, Wang Y, Warren MS, Condeelis JS, Koleske AJ. Arg/Abl2 promotes invasion and attenuates proliferation of breast cancer in vivo. Oncogene. 2013; 32:2622–2630. doi: 10.1038/onc.2012.284 PMID: 22777352

40. Jain HV, Clinton SK, Bhinder A, Friedman A. Mathematical modeling of prostate cancer progression in response to androgen ablation therapy. Proc Natl Acad Sci USA. 2011; 108(49):19701–6. doi: 10.1073/pnas.1115750108 PMID: 22106268

41. Weaver B. How Taxol/paclitaxel kills cancer cells. Mol Biol Cell. 2014; 25(18):2677–81. doi: 10.1091/mbc.E14-04-0916 PMID: 25213191

42. Yung BC, Li J, Zhang M, Cheng X, Li H, Yung EM, et al. Lipid Nanoparticles Composed of Quaternary Amine-Tertiary Amine Cationic Lipid Combination (QTsome) for Therapeutic Delivery of AntimiR-21 for Lung Cancer. Mol Pharmaceutics. 2016; 13(2):653–662. doi: 10.1021/acs.molpharmaceut.5b00878 PMID: 26741162

43. Tamura K, Fukuoka M. Gefitinib in non-small cell lung cancer. Expert Opin Pharmacother. 2005; 6 (6):985–93. doi: 10.1517/14656566.6.6.985 PMID: 15952926

44. Sharma SV, Bell DW, Settleman J, Haber DA. Epidermal growth factor receptor mutations in lung cancer. Nat Rev Cancer. 2007; 7(3):169–81. doi: 10.1038/nrc2088 PMID: 17318210

45. Jo U, Park KH, Whang YM, Sung JS, Won NH, Park JK, et al. EGFR endocytosis is a novel therapeutic target in lung cancer with wild-type EGFR. Oncotarget. 2014; 5(5):1265–78. doi: 10.18632/oncotarget.1711 PMID: 24658031

46. Florea AM, Busselberg D. Cisplatin as an anti-tumor Drug: Cellular mechanisms of activity, drug resistance and induced side effects. Cancers. 2011; 3(1):1351–1371. doi: 10.3390/cancers3011351 PMID: 24212665

47. Sorkin A, Duex JE. Quantitative analysis of endocytosis and turnover of epidermal growth factor (EGF) and EGF receptor. Curr Protoc Cell Biol. 2010; 15(14). doi: 10.1002/0471143030.cb1514s46 PMID: 20235100

48. Fujioka A, Terai K, Itoh RE, Aoki K, Nakamura T, et al. Dynamics of the Ras/ERK MAPK cascade as monitored by fluorescent probes. J Biol Chem. 2006; 281(13):8917–8926. doi: 10.1074/jbc.M509344200 PMID: 16418172

49. Roskoski RJ. ERK1/2 MAP kinases: Structure, function, and regulation. Pharmacological Research. 2012; 66:105–143. doi: 10.1016/j.phrs.2012.04.005 PMID: 22569528

50. Kaur H, Park CS, Lewis JM, Haugh JM. Quantitative model of Ras-phosphoinositide 3-kinase signalling cross-talk based in co-operative molecular assembly. Biochem J. 2006; 393:235–243. doi: 10.1042/BJ20051022 PMID: 16159314

51. Callans L, Naama H, Khandelwal M, Plotkin R, Jardines L. Raf-1 Protein Expression in Human Breast Cancer Cells. Annals of Surgical Oncology. 1995; 2(1):38–42. doi: 10.1007/BF02303700 PMID: 7834453

52. Akinleye A, Furqan M, Mukhi N, Ravella P, Liu D. MEK and the inhibitors: from bench to bedside. J Hematol Oncol. 2013; 6:27. doi: 10.1186/1756-8722-6-27 PMID: 23587417

53. Legewie S, Herzel H, Westerhoff H, Bluthgen N. Recurrent design patterns in the feedback regulation of the mammalian signalling network. Mol Syst Biol. 2008; 17:190. doi: 10.1038/msb.2008.29 PMID: 18463614

54. Leander R, Dai S, Schlesinger LS, Friedman A. A mathematical model of CR3/TLR2 crosstalk in the context of francisella tularensis infection. PLOS Compt Biol. 2012; 8(11):e1002757. doi: 10.1371/journal.pcbi.1002757

55. Cantrell DA. Phosphoinositide 3-kinase signalling pathways. J Cell Sci. 2001; 114(8):1439–45. PMID: 11282020

56. Meyer R, D'Alessandro LA, Kar S, Kramer B, She B, Kaschek D, et al. Heterogeneous kinetics of AKT signaling in individual cells are accounted for by variable protein concentration. Front Physiol. 2012; 3:1–14. doi: 10.3389/fphys.2012.00451 PMID: 23226133

57. Reubold T, Wohlgemuth S, Eschenburg S. A new model for the transition of APAF-1 from inactive monomer to caspase-activating apoptosome. J Biol Chem. 2009; 284(47):32717–24. doi: 10.1074/jbc.M109.014027 PMID: 19801675

58. Riches A, Campbell E, Borger E, Powis S. Regulation of exosome release from mammary epithelial and breast cancer cells—a new regulatory pathway. Eur J Cancer. 2014; 50(5):1025–34. doi: 10.1016/j.ejca.2013.12.019 PMID: 24462375

59. Komatsu S, Ichikawa D, Takeshita H, Tsujiura M, Morimura R, Nagata H, et al. Circulating microRNAs in plasma of patients with oesophageal squamous cell carcinoma. Br J Cancer. 2011; 105(1):104–111. doi: 10.1038/bjc.2011.198 PMID: 21673684

60. Komatsu S, Ichikawa D, Tsujiura M, Konishi H, Takeshita H, Nagata H, et al. Prognostic impact of circulating miR-21 in the plasma of patients with gastric carcinoma. Anticancer Res. 2013; 33(1):271–6. PMID: 23267156

61. Bader AG, Brown D, Stoudemire J, Lammers P. Developing therapeutic microRNAs for cancer. Gene Therapy. 2011; 18:1121–1126. doi: 10.1038/gt.2011.79 PMID: 21633392

62. Szomolay B, Eubank T, Roberts RD, Marsh CB, Friedman A. Modeling the inhibition of breast cancer growth by GM-CSF. J Theor Biol. 2012; 303:141–151. doi: 10.1016/j.jtbi.2012.03.024 PMID: 22763136

63. Shukla S, Allam US, Ahsan A, Chen G, Krishnamurthy PM, Marsh K, et al. KRAS protein stability is regulated through SMURF2: UBCH5 complex-mediated β-TrCP1 degradation. Neoplasia. 2014; 16:115–128. doi: 10.1593/neo.14184 PMID: 24709419

64. Schumacher C, Cioffi CL, Sharif H, Haston W, Monia BP, Wennogle L, et al. Exposure of human vascular smooth muscle cells to Raf-1 antisense oligodeoxynucleotides: cellular responses and pharmacodynamic implications. Mol Pharmacol. 1998; 53(1):97–104. PMID: 9443936

65. Wang PY, Rao JN, Zou T, Liu L, Xiao L, Yu TX, et al. Posttranscriptional regulation of MEK-1 by polyamines through the RNA-binding protein HuR modulating intestinal epithelial apoptosis. Biochem J. 2010; 426(3):293–306. doi: 10.1042/BJ20091459 PMID: 20001965

66. Satoh M, Parent AD, Zhang JH. Inhibitory Effect With Antisense Mitogen-Activated Protein Kinase Oligodeoxynucleotide Against Cerebral Vasospasm in Rats. Stroke. 2002; 33:775–781. doi: 10.1161/hs0302.103734 PMID: 11872903

67. Lee JH, Shin SH, Kang S, Lee YS, Bae S. A novel activation-induced suicidal degradation mechanism for Akt by selenium. Int J Mol Med. 2008; 21(1):91–7. PMID: 18097621

68. Basso AD, Solit DB, Chiosis G, Giri B, Tsichlis P, Rosen N. Akt Forms an Intracellular Complex with Heat Shock Protein 90 (Hsp90) and Cdc37 and Is Destabilized by Inhibitors of Hsp90 Function. J Biol Chem. 2002; 277(42):39858–66. doi: 10.1074/jbc.M206322200 PMID: 12176997

69. Peters S, Zimmermann S, Adjei AA. Oral epidermal growth factor receptor tyrosine kinase inhibitors for the treatment of non-small cell lung cancer: Comparative pharmacokinetics and drug-drug interactions. Cancer Treatment Reviews. 2014; 40:917–926. doi: 10.1016/j.ctrv.2014.06.010 PMID: 25027951

70. Faratian D, Goltsov A, Lebedeva G, Sorokin A, Moodie S, Mullen P, et al. Systems biology reveals new strategies for personalizing cancer medicine and confirms the role of PTEN in resistance to trastuzumab. Cancer Res. 2009; 69(16):6713–20. doi: 10.1158/0008-5472.CAN-09-0777 PMID: 19638581

71. Vazquez F, Ramaswamy S, Nakamura N, Sellers WR. Phosphorylation of the PTEN tail regulates protein stability and function. Mol Cell Biol. 2000; 20(14):5010–8. doi: 10.1128/MCB.20.14.5010-5018.2000 PMID: 10866658

72. Vreeland AC, Yu S, Levi L, de Barros Rossetto D, Noya N. Transcript Stabilization by the RNA-Binding Protein HuR Is Regulated by Cellular Retinoic Acid-Binding Protein 2. Molecular and Cellular Biology. 2014; 34(12):2135–2146. doi: 10.1128/MCB.00281-14 PMID: 24687854

73. von Roretz C, Lian XJ, Macri AM, Punjani N, Clair E, Drouin O, et al. Apoptotic-induced cleavage shifts HuR from being a promoter of survival to an activator of caspase-mediated apoptosis. Cell Death Differ. 2013; 20:154–168. doi: 10.1038/cdd.2012.111 PMID: 22955946

74. McDonald D. Understanding miRNA turnover: a study of miRNA lalf-life. Broad Insitute. 2010;.

75. Dearden S, Stevens J, Wu YL, Blowers D. Mutation incidence and coincidence in non small-cell lung cancer: meta-analyses by ethnicity and histology (mutMap). Annals of Oncology. 2013; 24:2371–2376. doi: 10.1093/annonc/mdt205 PMID: 23723294

76. Lung Cancer Mutation Panel (EGFR, KRAS, ALK). Quest Diagnosis; Available from: http://www.questdiagnostics.com/testcenter/TestDetail.action?ntc=91216

77. Liao KL, Bai XF, Friedman A. Mathematical modeling of interleukin-27 induction of anti-tumor T cells response. PLoS ONE. 2014; 9(3):e91844. doi: 10.1371/journal.pone.0091844 PMID: 24633175

78. McIlwain DR, Berger T, Mak TW. Caspase functions in cell death and disease. Cold Spring Harb Perspect Biol. 2013; 5(4):a008656. doi: 10.1101/cshperspect.a008656 PMID: 23545416

79. Young ME. Estimation of diffusion coefficients of proteins. Biotechnology and Bioengineering. 1980; XXII:947–955. doi: 10.1002/bit.260220504

80. Shui YB, Wang X, Hu JS, Wang SP, Garcia CM, Potts JD, et al. Vascular endothelial growth factor expression and signaling in the lens. Invest Ophthalmol Vis Sci. 2003; 44(9):3911–9. doi: 10.1167/iovs.02-1226 PMID: 12939309

81. Marino S, Hogue IB, Ray CJ, Kirschner DE. A methodology for performing global uncertainty and sensitivity analysis in systems biology. J Theor Biol. 2008; 254(1):178–96. doi: 10.1016/j.jtbi.2008.04.011 PMID: 18572196

82. Hao W, Crouser ED, Friedman A. Mathematical model of sarcoidosis. Proc Natl Acad Sci USA. 2014; 111(45):16065–70. doi: 10.1073/pnas.1417789111 PMID: 25349384

83. Hao W, Friedman A. The LDL-HDL Profile Determines the Risk of Atherosclerosis: A Mathematical Model. PLoS ONE. 2014; 9(3):e90497. doi: 10.1371/journal.pone.0090497 PMID: 24621857